NAVIGATION USING INERTIAL SENSORS

Paul D. Groves
University College London
United Kingdom
p.groves@ucl.ac.uk

Abstract

This tutorial provides an introduction to navigation using inertial sensors, explaining the underlying principles. Topics covered include accelerometer and gyro technology and their characteristics, strapdown inertial navigation, attitude determination, integration and alignment, zero updates, motion constraints, pedestrian dead reckoning using step detection, and fault detection.

Index Terms

Navigation, Inertial Navigation, Integrated Navigation

I. INTRODUCTION

Inertial sensors comprise accelerometers, which measure specific force, and gyroscopes, commonly abbreviated to gyros, which measure angular rate. An inertial measurement unit (IMU) combines multiple accelerometers and gyros, usually three of each, to produce three-dimensional measurements of specific force and angular rate. By integrating these measurements and applying a gravity model, a position, velocity, and attitude solution may be maintained, a concept known as inertial navigation.

Practical inertial navigation systems (INS) have been available from the 1950s, but were initially very large and expensive. In early INS, the sensors were physically aligned with the horizontal and vertical by mounting them on a platform connected to the host body by a series of gimbals driven by motors. This was known as a platform configuration and was due to the limitations of early gyro technology and the need to minimize the computational load. The strapdown configuration, whereby the sensors are aligned with the host body, was first proposed in 1962 [1] with production of the first aircraft systems starting at the end of the 1970s [2]. Today, it is almost universal. Inertial sensors are now available with a wide range of physical and performance characteristics at costs ranging from a few dollars to hundreds of thousands of dollars.

This tutorial provides an introduction to navigation using inertial sensors, covering a range of topics and explaining the underlying principles. Section II describes how accelerometers and gyros work and introduces the IMU. Section III then reviews their error characteristics. Strapdown inertial navigation is explained in Section IV, including the basic principles, initialization, the navigation equations, and error propagation. Section V then describes absolute attitude determination using inertial sensors, both alone and with magnetometers. Section VI explains how inertial navigation performance is improved through integration with other sensors. Section VII then introduces zero updates and motion constraints. Section VIII introduces pedestrian dead reckoning using step detection, an alternative navigation technique.

Finally Section IX discusses fault detection and Section X presents concluding remarks.

The notation, conventions, and terminology are based on [3], which provides further details of most of the topics covered.

II. INERTIAL SENSORS

This section describes the basic principles of the accelerometer and gyro, compares the different types of sensor, and then explains how they are incorporated into an inertial measurement unit. Inertial sensor technology is described in more detail in [3–5].

A. Accelerometers

Figure 1 shows a simple accelerometer. A proof mass is free to move with respect to the accelerometer case along the accelerometer's sensitive axis, restrained by springs. A pickoff measures the position of the mass with respect to the case. When an accelerating force along the sensitive axis is applied to the case, the proof mass will initially continue at its previous velocity, so the case will move with respect to the mass, compressing one spring and stretching the other. This alters the forces the springs transmit. Consequently, the case will move with respect to the mass until the acceleration of the mass due to the asymmetric forces exerted by the springs matches the acceleration of the case due to the externally applied force. The resultant position of the mass with respect to the case is proportional to the applied acceleration. By measuring this with a pickoff, an acceleration measurement is obtained.
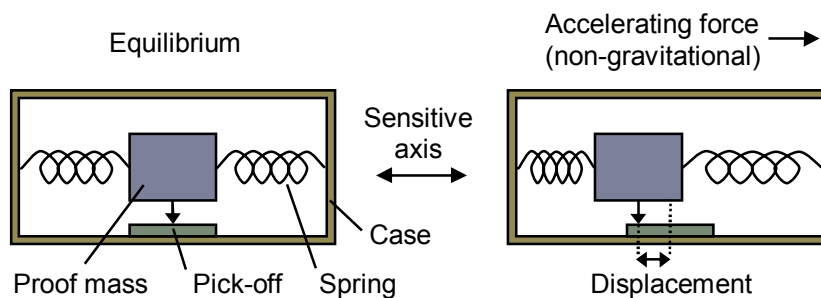

Figure 1. A simple accelerometer (From [3] © Paul Groves 2013. Reproduced with Permission).

An important exception is gravitational acceleration. This acts on the proof mass directly, not via the springs, and applies the same acceleration to all components of the accelerometer, so there is no relative motion of the mass with respect to the case. Therefore, accelerometers sense only the nongravitational acceleration, known as specific force. People also sense specific force. The sensation of weight is actually caused by the forces opposing gravity, known as the restoring force on land, buoyancy at sea, and lift in the air. During freefall, the specific force is zero so there is no sensation of weight. Conversely, under zero acceleration when the specific force is equal and opposite to the acceleration due to gravity, the reaction to gravity is sensed as weight.

An accelerometer measures the specific force of the accelerometer case with respect to inertial space, which does not accelerate or rotate with respect to the rest of the universe. An IMU containing a triad of accelerometers with mutually-orthogonal sensitive axes measures the specific force vector, $\mathbf{f}_{ib}^{b}$, where the subscript *ib* denotes measurement of the origin of the IMU body frame, *b*, with respect to an inertial frame, *i*, and the superscript *b* denotes that the components of the vector are resolved along the axes of the IMU body frame, which normally coincide with the sensitive axes of the constituent sensors (an exception is the skewed configuration; see Section IX). The specific force may be expressed in terms of the inertially referenced acceleration, $\mathbf{a}_{ib}^{b}$, and the gravitational acceleration, $\boldsymbol{\gamma}_{ib}^{b}$, using

$$\mathbf{f}_{ib}^{b} = \mathbf{a}_{ib}^{b} - \boldsymbol{\gamma}_{ib}^{b} \ . \tag{1}$$

However, it is often more convenient to express the specific force in terms of the Earth referenced acceleration, $\mathbf{a}_{eb}^{b}$. Thus,

$$\mathbf{f}_{ib}^{b} = \mathbf{a}_{eb}^{b} - \mathbf{g}_{b}^{b} \ , \tag{2}$$

where $\mathbf{g}_{b}^{b}$ is the acceleration due to gravity, the sum of the gravitational acceleration and the outward centrifugal acceleration due to the Earth's rotation. Centrifugal acceleration is a pseudo-acceleration arising from the use of a rotating reference frame [3].

The accelerometer hardware shown in Figure 1 is incomplete. The proof mass must be supported in the axes perpendicular to the sensitive axis, and damping is needed to limit oscillation of the proof mass. Practical accelerometers used for navigation currently follow either a pendulous or vibrating-beam design.

In a pendulous accelerometer, the proof mass is attached to the case via a pendulous arm and hinge, forming a pendulum. This leaves the proof mass free to move along the sensitive axis while supporting it in the other two axes. The hinge provides damping, which may be increased by filling the case with oil. In an open-loop pendulous accelerometer, one or two springs are used to transmit force from the case to the pendulum along the sensitive axis. However, the accuracy is limited by the pickoff resolution, the nonlinearity of the spring, and variation in the direction of the sensitive axis as the pendulum moves. Precision pendulous accelerometers therefore use a closed-loop, or force-feedback, configuration, whereby a torquer maintains the pendulous arm at a constant position with respect to the case [4, 5]. The pickoff detects departures from the equilibrium position as the specific force changes, and the torquer is adjusted to return the pendulum to that position. It is then the force exerted by the torquer, not the pickoff signal, which is proportional to the specific force.

Higher performance pendulous accelerometers are mechanical. Different grades of performance are offered at different prices by varying the component quality. Micro-electro-mechanical systems (MEMS) technology enables small and light quartz and silicon sensors to be mass produced at low cost using etching techniques with several sensors on a single wafer, offering a lower cost, lower performance alternative [6]. MEMS sensors also exhibit much greater shock tolerance than conventional designs, enabling them to be used in gun-launched guided munitions [7].

In a vibrating-beam accelerometer (VBA), the proof mass is also mounted on a pendulous arm. However, it is supported along the sensitive axis by a vibrating beam,

largely constraining its motion. When a force is applied to the accelerometer case along the sensitive axis, the beam pushes or pulls the proof mass, causing the beam to be compressed in the former case and stretched in the latter. This changes the resonant frequency of the beam. Therefore, by measuring this, the specific force along the sensitive axis can be determined. Performance is improved by using a pair of vibrating beams, arranged such that one is compressed while the other is stretched. Larger, higher performance VBAs use quartz, while lower cost MEMS VBAs can use quartz or silicon.

A third class of accelerometer, currently under development, is based on cold-atom interferometry [8, 9]. This offers a much higher precision than conventional sensors, but is relatively large and expensive, limiting its deployment to larger ships, submarines, and aircraft.

The operating range of an accelerometer is typically quoted in terms of the acceleration due to gravity, abbreviated to 'g', where 1g = 9.80665 m s^{-2}, noting that the actual acceleration due to gravity varies with location. Many navigation applications require an operational range of at least ±10g.

B. Gyroscopes

A device that senses angular rate with respect to inertial space is known as a gyroscope. Early gyroscopes used spinning mass technology. However, the vast majority of gyros used for navigation today are either optical or vibratory. An IMU containing a triad of gyros with mutually-orthogonal sensitive axes measures the angular rate vector, $\boldsymbol{\omega}_{ib}^{b}$, where the subscript *ib* denotes measurement of the axes of the IMU body frame with respect to an inertial frame and the superscript *b* denotes that the components of the vector are resolved about the axes of the IMU body frame, which normally coincide with the gyro sensitive axes. Manned vehicles typically rotate at up to 3 rad s^{-1} (170 deg s^{-1}) [10]. However, a gun-launched guided shell can rotate at up to 120 rad s^{-1} (6,800 deg s^{-1}) [7].

1) *Optical gyroscopes.* Optical gyroscopes work on the principle that, in a given medium, light travels at a constant speed in an inertial frame. If light is sent in both directions around a nonrotating closed-loop waveguide made of mirrors or optical fiber, the path length is the same for both beams. However, if the waveguide is rotated within its plane, then, from the perspective of an inertial frame, the reflecting surfaces are moving further apart for light traveling in the same direction as the rotation and closer together for light traveling in the opposite direction. Thus, rotating the waveguide in the same direction as the light path increases the path length and rotating it in the opposite direction decreases the path length. This is known as the Sagnac effect and is illustrated by Figure 2. By measuring the changes in path length, the angular rate of the waveguide with respect to inertial space can be determined.

No rotation | Rotation in same direction as light – path length increases | Rotation in opposite direction to light – path length decreases
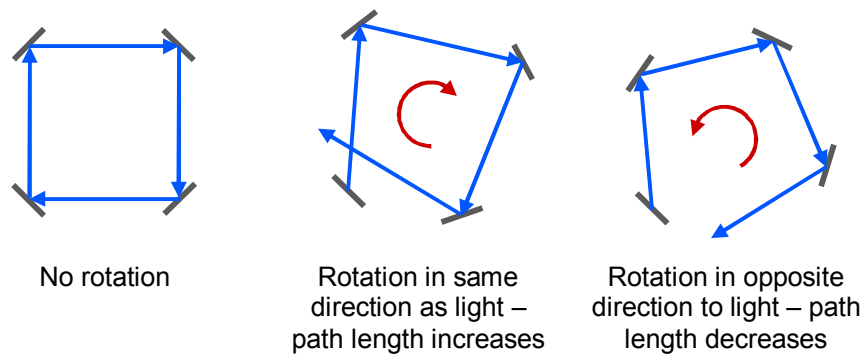
Figure 2 . Effect of closed-loop waveguide rotation on path length. (From [3] © Paul Groves 2013. Reproduced with Permission).

There are two main types of optical gyro. The ring laser gyro (RLG) was originally designed as a high-performance technology with the interferometric fiber-optic gyro (IFOG) as a lower cost solution. However, the performance ranges now overlap with IFOGs able to meet the performance standards for civil and military aviation.

In a ring laser gyro, light travels in both directions around a closed-loop tube, known as a laser cavity, containing a helium-neon gas mixture. The cavity comprises at least three arms with a mirror at each corner. The wavelength of the light depends on both the properties of the gas and the length of the laser cavity, which must contain an integer number of wavelengths. If the laser cavity does not rotate, the light travelling in each direction has the same wavelength. However, if the laser cavity is rotated within its plane, the cavity length is increased for light travelling in the direction of rotation and decreased for the light travelling in the opposite direction, changing both wavelengths. Light traveling in both directions is focused on a detector and the angular rate is deduced from the interference pattern.

In an interferometric fiber-optic gyro, broadband light is modulated and split into two equal portions that are then sent through a fiber-optic coil in opposite directions. Within the coil, light travelling in one direction is lagged or advanced with respect to light travelling in the other direction according to the angular rate of the coil within its plane. The outputs from the coil are recombined and passed to a detector which measures the interference between them, from which the angular rate may be deduced.

2) *Vibratory Gyroscopes*. A vibratory gyroscope is based around a driven vibrating element, which may be a string, beam, pair of beams, tuning fork, ring, cylinder, or hemisphere. The Coriolis acceleration of the vibrating element is detected when the gyro is rotated. Figure 3 illustrates this for a vibrating string. This is able to vibrate in two orthogonal directions and is driven to vibrate along one of these directions. If the string is then rotated about its longitudinal axis, which is perpendicular to the directions it can vibrate along, the Coriolis effect induces vibration along the axis perpendicular to both the drive and longitudinal axes. The amplitude of this vibration is proportional to the angular rate.
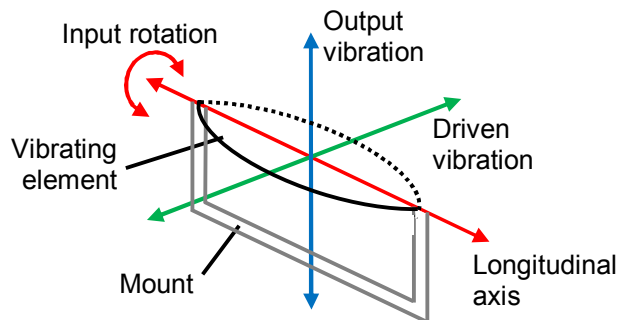
Figure 3. Axes of a vibrating gyro.

Most vibratory gyros are low-cost, low-performance devices, often using MEMS technology [6] and with quartz giving better performance than silicon. The exception is the hemispherical resonator gyro (HRG), which can offer aviation grade performance and is often used for space applications.

3) *Other types of Gyroscope.* Traditional spinning-mass gyroscopes remain in use in old equipment while a number of new technologies for sensing angular rate are under development. Nuclear magnetic resonance (NMR) gyro technology has now been developed on a chip scale, offering high performance with small and light sensors [11]. Cold-atom interferometry offers the potential of much higher precision than current gyroscope technology for large-scale applications [12]. In theory, angular rate can also be sensed using an array of accelerometers [13]. However, this is not currently a practical solution.

C. Inertial Measurement Units

Figure 4 shows the main elements of a typical inertial measurement unit. The IMU regulates the power supplies to the accelerometers and gyroscopes, digitizes their outputs, and transmits them on a data bus. The specific forces and angular rates, or their integrals (known as "delta-v"s and "delta-θ"s) are output at a rate between 100 and 1,000 Hz. Most IMUs have three accelerometers and three gyroscopes, mounted with orthogonal sensitive axes. However, some incorporate additional inertial sensors in a skewed configuration to protect against single sensor failure (see Section IX). Conversely, for some land vehicle applications, partial IMUs, comprising three accelerometers and a single yaw-axis gyro, are used [14].
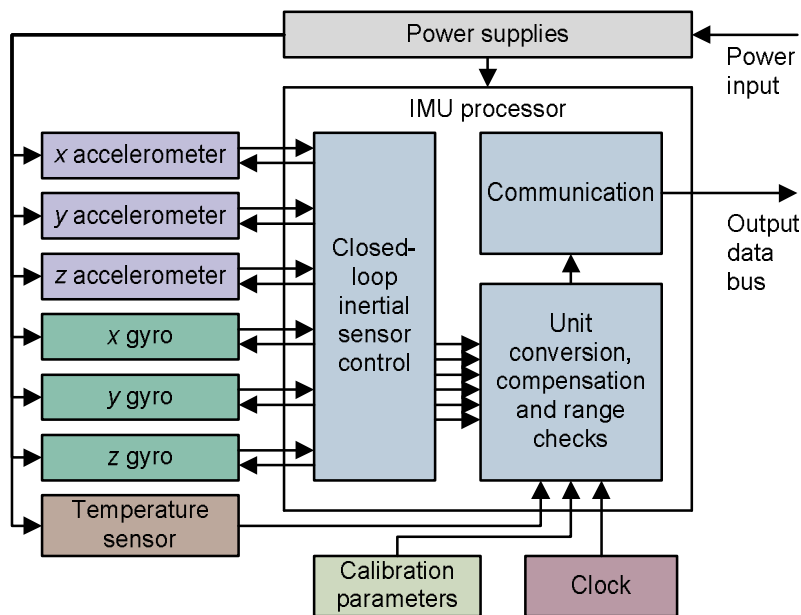
Figure 4. Schematic of an inertial measurement unit. (From [3] © Paul Groves 2013. Reproduced with Permission).

Inertial sensors exhibit systematic errors (see Section III) which can be calibrated in the laboratory and stored in memory, enabling the IMU processor to correct the sensor outputs. These errors vary with temperature, so the calibration is performed at a range of temperatures and the IMU is equipped with a temperature sensor.

Inertial sensors are sensitive to vibration (e.g., from a propulsion system). Many IMUs therefore incorporate vibration isolators, which also protect the components from shock. These must be designed to limit the transmission of vibrations at frequencies (and harmonics thereof) close to either the mechanical resonances of the sensors or the computational update rates of the IMU [4, 10].

There is no universally agreed definition of high-, medium-, and low-grade inertial sensors. One author's medium grade can be another's high or low grade. IMUs, INSs, and inertial sensors may be grouped into five broad performance categories: marine, aviation, intermediate, tactical, and consumer.

The highest quality sensors are used in military ships, submarines, some inter-continental ballistic missiles, and some spacecraft, noting that different sensors are required for these very different environments. A *marine-grade* INS can cost in excess of a million dollars.

Aviation-grade, or navigation-grade INSs are used in military aircraft and commercial airliners. They cost around $100,000, have a standard size of $178 \times 178 \times 249$ mm, and must exhibit a horizontal position drift within 1.5 km in the first hour of operation. An intermediate-grade IMU, about an order of magnitude poorer in performance, is used in smaller aircraft and helicopters and costs $20,000–50,000.

A tactical-grade IMU can only be used for stand-alone inertial navigation solution for a few minutes. However, an accurate long-term navigation solution can be obtained by integrating it with a positioning system, such as GPS. These IMUs typically cost between $2,000 and $30,000 and are used in guided weapons and

unmanned air vehicles (UAVs). Most are less than a liter in volume. Tactical grade covers a wide span of sensor performance, particularly for gyros.

The lowest grade of inertial sensors are known as consumer grade or automotive grade. They are usually supplied as individual sensors or accelerometer and gyro triads, rather than as complete IMUs. Without calibration, they are not accurate enough for inertial navigation, even when integrated with other navigation systems, but can be used for attitude determination, detection of a pedestrian's steps, and detection of context information, such as vehicle type and activity. They are typically used in pedometers, antilock braking, active suspension, and airbags. Accelerometers cost around a dollar or euro while gyro prices start at about $10. Sensors can be as small as 5×5×1 mm.

The extent of calibration and other processing applied within the IMU can affect performance dramatically, particularly for MEMS sensors [15]. Sometimes, the same MEMS inertial sensors are sold at consumer grade without calibration and tactical grade with calibration.

III. SENSOR ERROR CHARACTERISTICS

All types of accelerometer and gyro exhibit biases, scale factor and cross-coupling errors, and random noise to a certain extent. Further errors may also arise, depending on the sensor type. Each of these errors is discussed in turn, followed by a summary error model. Further details may be found in [3, 4, 10].

Each systematic error source has four components: a fixed contribution, a temperature-dependent variation, a run-to-run variation, and an in-run variation. The fixed contribution is present each time the sensor is used and is normally corrected by the IMU processor using the laboratory calibration data. The temperature-dependent component can be similarly corrected. Otherwise, the systematic errors will typically vary over the first few minutes of operation as the sensor warms up to its normal operating temperature.

The run-to-run variation of each error source results in a contribution to the total error which is different each time the sensor is used, but remains constant within any run. The in-run variation contribution changes slowly during the course of a run. Neither can be corrected by the IMU processor, but they can be calibrated through integration with other navigation sensors as described in Section VI. Sudden step changes in the systematic errors can also occur if an IMU is subject to a large shock, such as launching it from a gun [7].

In discussing the error performance of different types of inertial sensor here, the contributions to the error sources that are corrected within the IMU are neglected as the postcalibration performance is of greatest interest.

A. Biases
The bias is a constant error exhibited by all accelerometers and gyros. It is independent of the underlying specific force and angular rate and is usually the largest error source. Accelerometer biases are typically quoted in units of milli-g (mg) or micro-g (μg), where $1g = 9.80665$ m s^{-2}, while, for gyro biases, degrees per hour ($°$ hr^{-1} or deg/hr) are normally used, where $1 °$ hr$^{-1} = 4.848×10^{-6}$ rad s^{-1}. Table 1 lists typical accelerometer and gyro biases for different grades of IMU [3].

Table 1. Typical Accelerometer and Gyro Biases for Different Grades of IMU.

IMU grade	Accelerometer bias		Gyro bias	
	mg	m s^{-2}	° hr^{-1}	rad s^{-1}
Marine	0.01	10^{-4}	0.001	5×10^{-9}
Aviation	0.03–0.1	3×10^{-4}–10^{-3}	0.01	5×10^{-8}
Intermediate	0.1–1	10^{-3}–10^{-2}	0.1	5×10^{-7}
Tactical	1–10	0.01–0.1	1–100	5×10^{-6}–5×10^{-4}
Consumer	>3	>0.03	>100	>5×10^{-4}

Pendulous accelerometers span most of the performance range, while VBAs exhibit biases of 0.1 mg upward, with MEMS accelerometers of both types exhibiting the largest biases. RLG biases vary from 0.001 ° hr^{-1} to 10 ° hr^{-1}, depending on the sensor quality, while IFOG biases range between 0.01 and 100 ° hr^{-1} and vibratory-gyro biases range from 1 ° hr^{-1} to 1 ° s^{-1}. Uncalibrated MEMS sensors can exhibit larger biases, including temperature- variations of several degrees per second or milli-g [16].

B. Scale Factor and Cross-Coupling Errors

The scale factor error is the departure of the input-output gradient of the instrument from unity. The resulting accelerometer error is thus proportional to the true specific force, while the gyro error is proportional to the true angular rate. The lowest-cost sensors can exhibit significant scale factor asymmetry, whereby the scale factor errors are different for positive and negative readings.

Cross-coupling errors make each accelerometer sensitive to the specific force along the axes orthogonal to its sensitive axis and each gyro sensitive to the angular rate about the axes orthogonal to its sensitive axis. One of the major causes is mounting misalignment, whereby the sensitive axes of the inertial sensors are not completely orthogonal due to manufacturing limitations. In vibratory sensors, cross-talk between the individual sensors can arise. In consumer-grade MEMS sensors, the cross-coupling errors of the sensor itself can dominate. Cross-coupling errors are sometimes called misalignment errors or cross-axis sensitivity.

Scale factor and cross-coupling errors are typically expressed in parts per million (ppm) or as a percentage, though some manufacturers quote the axis misalignments instead. The scale factor and cross-coupling errors of most types of inertial sensors, including IFOGs, are between 10^{-4} and 10^{-3} (100–1000 ppm). However, some uncalibrated consumer-grade MEMS sensors exhibit scale factor errors as high as 0.1 (10%) and cross-coupling errors of up to 0.02 (2%), while RLG scale factor errors are typically between 10^{-6} and 10^{-4} (1–100 ppm).

C. Random Noise

Accelerometers and gyros all exhibit random noise from both electrical and mechanical sources. This noise is approximately white for frequencies below 1 Hz, so the standard deviation of the average specific force and angular rate noise varies in inverse proportion to the square root of the averaging time. Consequently, the noise is often described using the root power spectral density (PSD) with units of µg/√Hz (=

9.80665 × 10^{-6} m $s^{-1.5}$) for accelerometer random noise and °/√hr (= 2.909 × 10^{-4} rad $s^{-0.5}$) for gyro random noise commonly used. The noise standard deviation is the corresponding root PSD multiplied by the square root of the sampling rate (or divided by the square root of the sampling interval). Thus, at a sampling rate of 400 Hz, an accelerometer noise PSD of 100 μg/√Hz corresponds to a noise standard deviation of 2 mg or 0.196 m s^{-2}. White random noise cannot be calibrated as there is no correlation between past and future values. MEMS sensors can also exhibit significant high-frequency noise, which can cause problems under high dynamics or high vibration.

The accelerometer and gyro random noise are sometimes described as random walks. This is because random noise on the specific force measurements is integrated to produce a random-walk error on the inertial velocity solution. Similarly, angular rate random noise is integrated to produce an attitude random-walk error. The standard deviation of a random-walk process is proportional to the square root of the integration time.

The accelerometer random-noise root PSD varies from about 20 μg/√Hz for aviation-grade IMUs, through about 100 μg/√Hz for tactical-grade IMUs, up to about 1000 μg/√Hz for consumer-grade MEMS sensors. Gyro random noise varies from 0.001–0.02 °/√hr for RLGs, through 0.03–0.1 °/√hr for tactical-grade IFOGs or quartz vibratory gyros, to 0.06–2 °/√hr for MEMS silicon vibratory gyros. For consumer-grade sensors, many manufacturers quote the standard deviation of the total noise (white and high frequency) at the sensor output rate instead of the root PSD. Noise levels of 2.5–10 mg for accelerometers and 0.3–1 °/s for gyros are common.

A further source of noise is the quantization of the IMU data-bus outputs. This rounds the sensor output to an integer multiple of a constant, known as the quantization level, as shown in Figure 5. The quantization errors are largest for consumer-grade sensors where the word length is typically 12 bits or less and they can have a similar impact to the noise of the sensors themselves. Thus, quantization errors can be as high as 10^{-3} m s^{-1} for integrated specific force increments and 2×10^{-5} rad for attitude increments.
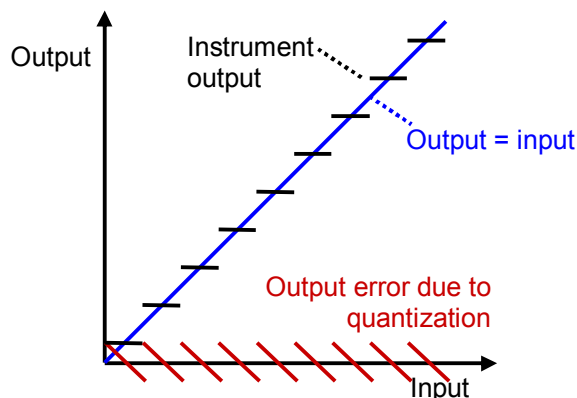

Figure 5. Effect of quantization on sensor output. (From [3] © Paul Groves 2013. Reproduced with Permission).

D. Further Error Sources

Inertial sensors often exhibit nonlinearity, whereby the scale factor varies with the specific force or angular rate. This is normally expressed as the variation of the scale factor over the operating range of the sensor and ranges from 10^{-5} for some RLGs, through 10^{-4} to 10^{-3} for most inertial sensors, to 10^{-2} for MEMS gyros. The largest nonlinearity effects typically occur at the maximum angular rates or specific forces that the sensor will measure.

Vibration interacts with the sensor scale factor and cross-coupling errors to produce oscillating sensor errors, which largely average to zero over time. However nonlinearity and/or asymmetry of the scale factor and cross-coupling errors results in a component of the vibration-induced sensor error that does not cancel. This is known as a vibration rectification error (VRE) and behaves like a bias that varies with the amplitude of the vibration.

Further error characteristics can be exhibited by certain types of accelerometer and gyro. Vibratory gyros and some IFOGs exhibit a sensitivity to the specific force along all three axes, known as the g-dependent bias. The coefficient is of order 1 °/hr/g (4.944×10^{-5} rad m^{-1} s) for an IFOG and 10–200 °/hr/g for an uncalibrated vibratory gyro [4]. Open-loop sensors, including some MEMS accelerometers and vibratory gyros, can also exhibit anisoinertia errors, whereby the cross-coupling errors vary as a function of the specific force or angular rate due to changes in the direction of the sensitive axis. These errors can interact vibration in the environment to produce a bias-like error known as the vibropendulous error.

MEMS sensors often exhibit errors due to their operating ranges being exceeded, in which case the sensor simply outputs its largest possible positive or negative reading. Note that human motion exceeds the maximum ranges of many consumer-grade sensors. Errors can also arise when the bandwidth of the sensor is exceeded, particularly for high-vibration environments.

E. Error Model

The contribution of the main error sources to the outputs of an accelerometer triad may be summarized by

$$\widetilde{\mathbf{f}}_{ib}^{b} = \mathbf{b}_a + \left(\mathbf{I}_3 + \mathbf{M}_a\right)\mathbf{f}_{ib}^{b} + \mathbf{w}_a, \tag{3}$$

where $\widetilde{\mathbf{f}}_{ib}^{b}$ is the IMU-output specific force vector, $\mathbf{b}_a$ is the accelerometer bias vector, $\mathbf{I}_3$ is the identity matrix, $\mathbf{M}_a$ is the matrix of coefficients of the accelerometer scale-factor error (diagonal elements) and cross-coupling error (off-diagonal elements), $\mathbf{f}_{ib}^{b}$ is the true specific force, and $\mathbf{w}_a$ is the accelerometer random noise vector.

Similarly, for a gyro triad,

$$\widetilde{\boldsymbol{\omega}}_{ib}^{b} = \mathbf{b}_g + \left(\mathbf{I}_3 + \mathbf{M}_g\right)\boldsymbol{\omega}_{ib}^{b} + \mathbf{G}_g\mathbf{f}_{ib}^{b} + \mathbf{w}_g, \tag{4}$$

where $\widetilde{\boldsymbol{\omega}}_{ib}^{b}$ is the IMU-output angular rate vector, $\mathbf{b}_g$ is the gyro bias vector, $\mathbf{M}_g$ is the matrix of gyro scale-factor error and cross-coupling error coefficients, $\mathbf{G}_g$ is the matrix of gyro g-dependent errors, $\boldsymbol{\omega}_{ib}^{b}$ is the true angular rate, and $\mathbf{w}_g$ is the gyro random noise vector.

IV. STRAPDOWN INERTIAL NAVIGATION

As shown in Figure 6, an inertial navigation system (INS) comprises an inertial measurement unit, described in Section II, and a navigation processor, which forms the focus of this section. The navigation processor computes a position, velocity, and attitude solution from the specific force and angular rate measurements made by the inertial sensors. For marine, aviation, and intermediate-grade systems, the IMU and navigation processor are typically packaged together. Where tactical or consumer-grade sensors are used, the navigation equations are typically implemented on an integrated navigation processor or the application's central processor.
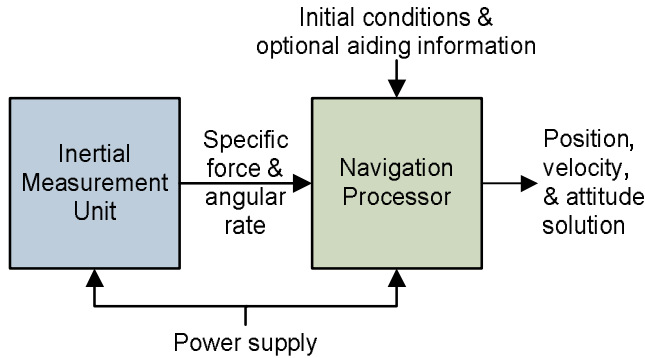

Figure 6. Basic schematic of an inertial navigation system. (From [3] © Paul Groves 2013. Reproduced with Permission).

The section begins by introducing inertial navigation, going from a single-dimensional implementation through two dimensions to three, followed by a discussion of initialization. The navigation equations are then described, with a derivation of the simplest form followed by the presentation of a more precise set of equations. Further implementations are described in [3, 4, 17, 18], including those using integrated specific force and attitude increments ("delta-v"s and "delta-θ"s). The section concludes by describing error propagation.

A. Introduction to Inertial Navigation

Considering first an example of one dimensional inertial navigation, a body, *b*, is constrained to move in a straight line perpendicular to the direction of gravity with respect to an Earth-fixed reference frame, *p*. The body's axes are fixed with respect to frame *p*, so it does not rotate. Its Earth-referenced acceleration may be measured by a single accelerometer with its sensitive axis aligned along the direction of motion (neglecting the Coriolis force).

If the speed, v_{pb}, is known at an earlier time, t_0, it may be determined at a later time, t, simply by integrating the acceleration, a_{pb}:

$$v_{pb}(t) = v_{pb}(t_0) + \int_{t_0}^{t} a_{pb}(t')dt' .$$

(5)

Similarly, the position may be obtained by integrating the velocity:

$$r_{pb}(t) = r_{pb}(t_0) + \int_{t_0}^{t} v_{pb}(t')dt'$$

$$= r_{pb}(t_0) + (t - t_0)v_{pb}(t_0) + \int_{t_0}^{t}\int_{t_0}^{t'} a_{pb}(t'')dt''dt'$$

(6)

Moving on to a two dimensional example, *b* is now constrained to move within a horizontal plane defined by the *x* and *y* axes of the *p* frame. It may be oriented in any direction within this plane, but is constrained to remain level. It thus has one angular and two linear degrees of freedom. Following, the 1D example, the position and velocity, resolved along the axes of the reference frame, *p*, are updated using

$$\begin{pmatrix} v_{pb,x}^{p}(t) \\ v_{pb,y}^{p}(t) \end{pmatrix} = \begin{pmatrix} v_{pb,x}^{p}(t_0) \\ v_{pb,y}^{p}(t_0) \end{pmatrix} + \int_{t_0}^{t} \begin{pmatrix} a_{pb,x}^{p}(t') \\ a_{pb,y}^{p}(t') \end{pmatrix} dt',$$

(7)

$$\begin{pmatrix} x_{pb}^{p}(t) \\ y_{pb}^{p}(t) \end{pmatrix} = \begin{pmatrix} x_{pb}^{p}(t_0) \\ y_{pb}^{p}(t_0) \end{pmatrix} + \int_{t_0}^{t} \begin{pmatrix} v_{pb,x}^{p}(t') \\ v_{pb,y}^{p}(t') \end{pmatrix} dt'.$$

(8)

Measuring the acceleration along two orthogonal axes requires two accelerometers. However, their sensitive axes will be aligned with those of the body, *b*. To determine the acceleration along the axes of frame *p*, the heading of frame *b* with respect to frame *p*, ψ_{pb}, is required as shown in Figure 7. The resolving axes of the accelerometer measurements may be then be transformed using a 2×2 coordinate transformation matrix:

$$\begin{pmatrix} a_{pb,x}^{p}(t') \\ a_{pb,y}^{p}(t') \end{pmatrix} = \begin{pmatrix} \cos\psi_{pb}(t') & -\sin\psi_{pb}(t') \\ \sin\psi_{pb}(t') & \cos\psi_{pb}(t') \end{pmatrix} \begin{pmatrix} a_{pb,x}^{b}(t') \\ a_{pb,y}^{b}(t') \end{pmatrix}.$$
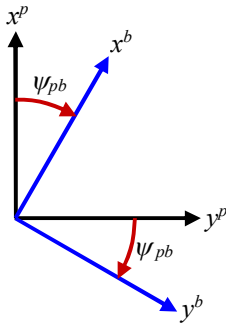
(9)

Figure 7. Orientation of body axes with respect to the resolving axes in a horizontal plane. (From [3] © Paul Groves 2013. Reproduced with Permission).

The rotation of the body, *b*, within the *xy* plane of the reference frame, *p*, may be measured with a single gyro with its sensitive axis perpendicular to the plane (neglecting Earth rotation). If the heading, ψ_{pb}, is known at the earlier time, t_0, it may be determined at the later time, *t*, by integrating the angular rate measured by the gyro, $\omega_{pb,z}^{b}$:

$$\psi_{pb}(t) = \psi_{pb}(t_0) + \int_{t_0}^{t} \omega_{pb,z}^{b}(t')dt'.$$

(10)

Three inertial sensors are thus required to measure the three degrees of freedom of motion in two dimensions.

For all practical applications, three-dimensional motion must be assumed. Even for land and marine navigation, strapdown inertial sensors will not remain in the horizontal plane due to terrain slopes or ship pitching and rolling. Consequently, nominally horizontal accelerometers will sense the reaction to gravity as well as the horizontal-plane acceleration. A platform tilt of 10 mrad (0.57°) produces an acceleration error of 0.1 m s^{-2}, leading to a position error 500m after 100s (see Section IV.E). Tilts of 10 times this are commonly exhibited by both cars and boats.

Unconstrained motion in three dimensions has six degrees of freedom, three linear and three angular, requiring six inertial sensors to measure it. The specific force, $\mathbf{f}_{ib}^{b}$, and angular rate, $\boldsymbol{\omega}_{ib}^{b}$, output by the IMU are integrated to produce an updated position, velocity, and attitude solution in four steps:

1. The attitude update;

2. The transformation of the specific-force resolving axes from the IMU body frame to the coordinate frame used to resolve the position and velocity;

3. The velocity update, including transformation of specific force into acceleration using a gravity or gravitation model; and

4. The position update.

Further details are presented in Sections IV.C and IV.D. Figure 8 summarizes this process. Note that the specific force and angular rate from the IMU are averaged over its sampling interval, whereas the position, velocity and attitude are applicable at the end of this interval. In an integrated navigation system, there may also be correction of the IMU outputs and navigation solution using estimates from the integration algorithm (see Section VI.E). Where a partial IMU is used, the missing angular rate measurements are assumed to be zero.
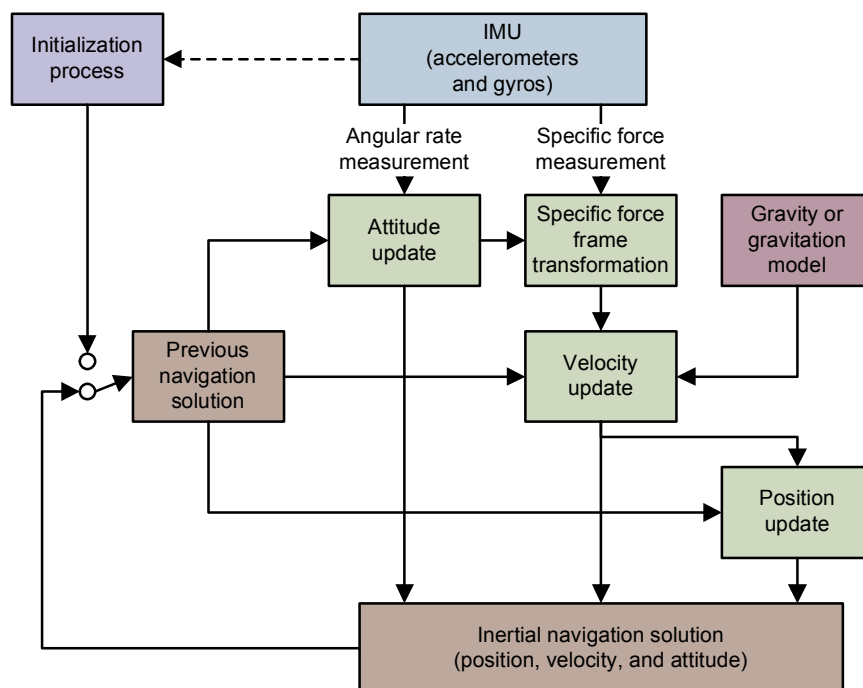
Figure 8. Schematic of an inertial navigation processor. (From [3] © Paul Groves 2013. Reproduced with Permission).

B. Initialization

As Figure 8 shows, each cycle of the inertial navigation equations uses the previous navigation solution as its starting point. Therefore, the position, velocity, and attitude solution must be initialized. Position and velocity initialization requires external information. The position can be initialized by starting at a known position. However, when inertial navigation forms part of an integrated navigation system (Section VI), another navigation technology, such as global navigation satellite systems (GNSS), is commonly used to initialize position.

Velocity may also be initialized from another navigation system. However, it is also common to set it to zero (with respect to the Earth) when the host vehicle is stationary. The effects of disturbance by wind or human activity, such as refueling and loading, may be minimized by performing the initialization process over several seconds, averaging out the motion effects.

When an INS is stationary, it can initialize its own attitude solution, a process known as self-alignment. The roll and pitch components of attitude are determined by measuring the direction of gravity using the accelerometers, a process known as leveling and described in Section V.A. The heading may be determined by measuring the rotation of the Earth using the gyros, which is known as gyrocompassing and described in Section V.B. However, effective gyrocompassing requires sensors of aviation grade or better. Otherwise, the heading must be initialized using external information. Magnetic heading measurement is described in Section V.C. Other methods, described in [3], include GNSS interferometric attitude determination, heading from trajectory, and image-based techniques.

C. Simple Inertial-Frame Navigation Equations

The simplest form of the inertial navigation equations computes a position, velocity and attitude with respect to, and resolved along the axes of, an Earth-centered inertial (ECI) coordinate frame. An ECI frame, denoted i, is an inertial frame with its origin at the Earth's center of mass. The z-axis points along the Earth's axis of rotation from the origin to the true north pole. The x- and y-axes lie within the equatorial plane, but do not rotate with the Earth. The y-axis points 90 degrees ahead of the x-axis in the direction of the Earth's rotation. An ECI-frame implementation is simplest because the inertial sensors measure motion with respect to an inertial frame so only two coordinate frames, the ECI frame and the body frame, are used. The effects of the Earth's rotation need not be considered. However, for most applications, the inertially-referenced navigation solution must be transformed to an Earth-referenced solution to be useful.

The four steps, described in turn in this subsection, show how the angular-rate and specific-force measurements made over the time interval t to $t + \tau_i$ are used to update the navigation solution. The suffixes (−) and (+) are, respectively, used to denote values at the beginning of the navigation equations processing cycle, at time t, and at the end of the processing cycle, at time $t + \tau_i$.

1) *Attitude Update.* The attitude update step of the inertial navigation equations uses the angular-rate measurement from the IMU, $\boldsymbol{\omega}_{ib}^b$, to update the attitude solution, expressed as the body-to-inertial-frame coordinate transformation matrix, $\mathbf{C}_b^i$. A coordinate transformation matrix, also known as a rotation matrix, is used to transform a vector from one set of resolving axes to another. Thus, for an arbitrary vector, $\mathbf{x}$,

$$\mathbf{x}^i = \mathbf{C}_b^i \mathbf{x}^b, \tag{11}$$

where the superscript of $\mathbf{x}$ denotes the resolving axes. The lower index of the coordinate transformation matrix represents the "from" frame and the upper index the "to" frame. Transformations are reversed simply by transposing the matrix, thus

$$\mathbf{C}_i^b = \mathbf{C}_b^{i\,\mathrm{T}}. \tag{11}$$

To perform successive transformations or rotations, the coordinate transformation matrices are simply multiplied:

$$\mathbf{C}_a^i = \mathbf{C}_b^i \mathbf{C}_a^b. \tag{12}$$

However, as with any matrix multiplication, the order is critical, so $\mathbf{C}_a^i \neq \mathbf{C}_a^b \mathbf{C}_b^i$. Performing a transformation and then reversing the process must return the original vector or matrix, so

$$\mathbf{C}_i^b \mathbf{C}_b^i = \mathbf{I}_3, \tag{13}$$

where $\mathbf{I}_n$ is the $n \times n$ identity or unit matrix. Coordinate transformation matrices are thus orthonormal and only 3 of the 9 components are independent. Although not always the most computationally efficient way of representing attitude, coordinate transformation matrices are comparatively straightforward and intuitive to manipulate.

As shown in [3, 19], the time derivative of the coordinate transformation matrix is

$$\dot{\mathbf{C}}_b^i = \mathbf{C}_b^i \boldsymbol{\Omega}_{ib}^b, \tag{14}$$

where $\boldsymbol{\Omega}_{ib}^b$ is the skew-symmetric matrix of the angular rate, defined as

$$\boldsymbol{\Omega}_{ib}^b = \left[\boldsymbol{\omega}_{ib}^b \wedge\right] = \begin{pmatrix} 0 & -\omega_{ib,z}^b & \omega_{ib,y}^b \\ \omega_{ib,z}^b & 0 & -\omega_{ib,x}^b \\ -\omega_{ib,y}^b & \omega_{ib,x}^b & 0 \end{pmatrix}. \tag{15}$$

Integrating (14) over the inertial navigation update interval gives

$$\mathbf{C}_b^i(t + \tau_i) = \mathbf{C}_b^i(t)\left[\lim_{n \to \infty} \prod_{i=1}^n \exp\left(\boldsymbol{\Omega}_{ib}^b\left(t + \frac{n-i}{n}\tau_i\right)\frac{\tau_i}{n}\right)\right], \tag{16}$$

If the angular rate is assumed to be constant over this interval, this simplifies to

$$\begin{aligned} \mathbf{C}_b^i(t + \tau_i) &\approx \mathbf{C}_b^i(t)\exp\left(\boldsymbol{\Omega}_{ib}^b \tau_i\right) \\ &= \mathbf{C}_b^i(t)\exp\left(\left[\boldsymbol{\omega}_{ib}^b \wedge\right]\tau_i\right), \\ &= \mathbf{C}_b^i(t)\exp\left[\left(\boldsymbol{\omega}_{ib}^b \tau_i\right)\wedge\right] \end{aligned} \tag{17}$$

noting that the exponent of a matrix is not the same as the matrix of the exponents of its components. Expressing (17) as a power series,

$$\mathbf{C}_b^i(t + \tau_i) = \mathbf{C}_b^i(t)\sum_{r=0}^{\infty} \frac{\left[\left(\boldsymbol{\omega}_{ib}^b \tau_i\right)\wedge\right]^r}{r!}. \tag{18}$$

The simplest form of attitude update is obtained by truncating the power-series to first order:

$$
\begin{aligned}
\mathbf{C}_b^i(+) &\approx \mathbf{C}_b^i(-)\left(\mathbf{I}_3 + \left[\left(\boldsymbol{\omega}_{ib}^b \tau_i\right)\wedge\right]\right) \\
&= \mathbf{C}_b^i(-)\left(\mathbf{I}_3 + \boldsymbol{\Omega}_{ib}^b \tau_i\right) \\
&= \mathbf{C}_b^i(-)\begin{pmatrix} 1 & -\omega_{ib,z}^b \tau_i & \omega_{ib,y}^b \tau_i \\ \omega_{ib,z}^b \tau_i & 1 & -\omega_{ib,x}^b \tau_i \\ -\omega_{ib,y}^b \tau_i & \omega_{ib,x}^b \tau_i & 1 \end{pmatrix}
\end{aligned}
\tag{19}
$$

This first-order approximation of (18) is a form of the small angle approximation, $\sin\theta \approx \theta$, $\cos\theta \approx 1$. It introduces errors in the attitude integration which will be larger at lower update rates (large τ_i) and higher angular rates. In practice, the first-order approximation can be used for land vehicle applications where the dynamics are low. However, for applications with high-dynamic, such as aviation, or regular periodic motion, such as pedestrian and boat navigation, a more precise attitude update is required, incorporating higher-order terms in the power series, (18).

2) *Specific-Force Frame Transformation.* The IMU measures specific force along the body-frame resolving axes. However, to use this to update the velocity solution, it must be resolved about the same axes as the velocity—in this case, an ECI frame. The resolving axes are transformed simply by applying a coordinate transformation matrix:

$$
\mathbf{f}_{ib}^i(t) = \mathbf{C}_b^i(t)\mathbf{f}_{ib}^b(t). \tag{20}
$$

As the specific-force measurement is an average over time t to $t + \tau_i$, the coordinate transformation matrix should be similarly averaged. A good approximation is

$$
\mathbf{f}_{ib}^i \approx \tfrac{1}{2}\left(\mathbf{C}_b^i(-) + \mathbf{C}_b^i(+)\right)\mathbf{f}_{ib}^b. \tag{20}
$$

3) *Velocity Update.* From (1), inertially referenced acceleration is obtained by adding the gravitational acceleration to the specific force:

$$
\mathbf{a}_{ib}^i = \mathbf{f}_{ib}^i + \boldsymbol{\gamma}_{ib}^i. \tag{21}
$$

The gravitational acceleration is determined using a model [20]:

$$
\boldsymbol{\gamma}_{ib}^i = -\frac{\mu}{\left|\mathbf{r}_{ib}^i\right|^3}\left\{\mathbf{r}_{ib}^i + \frac{3}{2}J_2\frac{R_0^2}{\left|\mathbf{r}_{ib}^i\right|^2}\left\{\begin{array}{c}\left[1 - 5\left(r_{ib,z}^i\big/\left|\mathbf{r}_{ib}^i\right|\right)^2\right]r_{ib,x}^i \\ \left[1 - 5\left(r_{ib,z}^i\big/\left|\mathbf{r}_{ib}^i\right|\right)^2\right]r_{ib,y}^i \\ \left[3 - 5\left(r_{ib,z}^i\big/\left|\mathbf{r}_{ib}^i\right|\right)^2\right]r_{ib,z}^i\end{array}\right\}\right\}, \tag{22}
$$

where $\mathbf{r}_{ib}^i$ is the Cartesian position of the IMU body frame with respect to the ECI frame origin, resolved along the ECI-frame axes, $R_0 = 6{,}378{,}137.0$ m is the Earth's equatorial radius, $\mu = 3.986004418\times10^{14}$ m³s⁻² is the Earth's gravitational constant, and $J_2 = 1.082627\times10^{-3}$ is the Earth's second gravitational constant [21].

The time derivative of the velocity of the IMU body frame with respect to the ECI frame origin, resolved along the ECI-frame axes, $\mathbf{v}_{ib}^i$, is simply the corresponding acceleration as the reference frame and resolving axes are the same. Thus,

$$\dot{\mathbf{v}}_{ib}^{i} = \mathbf{a}_{ib}^{i} . \tag{23}$$

The velocity is updated by integrating this. Assuming the acceleration is constant over the update interval gives

$$\mathbf{v}_{ib}^{i}(+) = \mathbf{v}_{ib}^{i}(-) + \mathbf{a}_{ib}^{i}\tau_{i} . \tag{24}$$

4) *Position Update.* As the reference frame and resolving axes are the same, the time derivative of the Cartesian position is simply the velocity. Thus,

$$\dot{\mathbf{r}}_{ib}^{i} = \mathbf{v}_{ib}^{i} . \tag{25}$$

Where the variation in acceleration over the update interval is unknown, $\mathbf{v}_{ib}^{i}$ is assumed to be a linear function of time over the interval t to $t + \tau_i$. The position may therefore be updated using

$$\mathbf{r}_{ib}^{i}(+) = \mathbf{r}_{ib}^{i}(-) + \left(\mathbf{v}_{ib}^{i}(-) + \mathbf{v}_{ib}^{i}(+)\right)\frac{\tau_i}{2} . \tag{26}$$

5) *Navigation Solution Transformation.* To obtain a navigation solution with respect to the Earth, a transformation is required. An Earth-centered Earth-fixed (ECEF) coordinate frame, denoted *e*, has its origin at the Earth's center of mass, coincident with the ECI-frame origin. The *z*-axis also points from origin to the true north pole. However, the *x*- and *y*-axes are fixed with respect to the Earth, rotating with it, with the *x*- and *y*-axes pointing from the origin to the 0° and 90° east meridians, respectively. The Cartesian ECEF position is obtained using

$$\mathbf{r}_{eb}^{e} = \mathbf{C}_{i}^{e}\mathbf{r}_{ib}^{i}, \quad \mathbf{C}_{i}^{e} = \begin{pmatrix} \cos\omega_{ie}(t-t_0) & \sin\omega_{ie}(t-t_0) & 0 \\ -\sin\omega_{ie}(t-t_0) & \cos\omega_{ie}(t-t_0) & 0 \\ 0 & 0 & 1 \end{pmatrix}, \tag{27}$$

where t_0 is the time at which the ECEF-frame and ECI-frame axes coincide and $\omega_{ie} = 7.292115 \times 10^{-5}$ rad s^{-1} is the Earth rotation rate [21].

For most applications, it is more convenient to express position with respect to the surface of the Earth rather than the center. The surface is irregular so, for navigation purposes, is typically approximated by an ellipsoid. The geodetic latitude of body *b*, L_b, is defined as the angle of intersection of the normal from *b* to the ellipsoid with the equatorial plane. The longitude, λ_b, is the angle subtended in the equatorial plane between the meridian plane containing *b* and the 0° meridian plane. Finally, the geodetic height, h_b, is the distance from *b* to the ellipsoid surface along the normal to that ellipsoid. Figure 9 illustrates this. Together, L_b, λ_b, and h_b form the curvilinear position of point *b*. This may be determined from the corresponding Cartesian position using [22]

$$\tan L_b \approx \frac{z_{eb}^e \sqrt{1-e^2} + e^2 R_0 \sin^3 \zeta_b}{\sqrt{1-e^2}\left(\sqrt{x_{eb}^{e\ 2} + y_{eb}^{e\ 2}} - e^2 R_0 \cos^3 \zeta_b\right)}$$

$$\tan \lambda_b = \frac{y_{eb}^e}{x_{eb}^e} \qquad (28)$$

$$h_b = \frac{\sqrt{x_{eb}^{e\ 2} + y_{eb}^{e\ 2}}}{\cos L_b} - R_E(L_b)$$

where $e = 0.0818191908425$ [21] is the eccentricity of the ellipsoid and

$$\tan \zeta_b = \frac{z_{eb}^e}{\sqrt{1-e^2}\sqrt{x_{eb}^{e\ 2} + y_{eb}^{e\ 2}}}, \qquad R_E(L_b) = \frac{R_0}{\sqrt{1-e^2 \sin^2 L_b}}, \qquad (29)$$

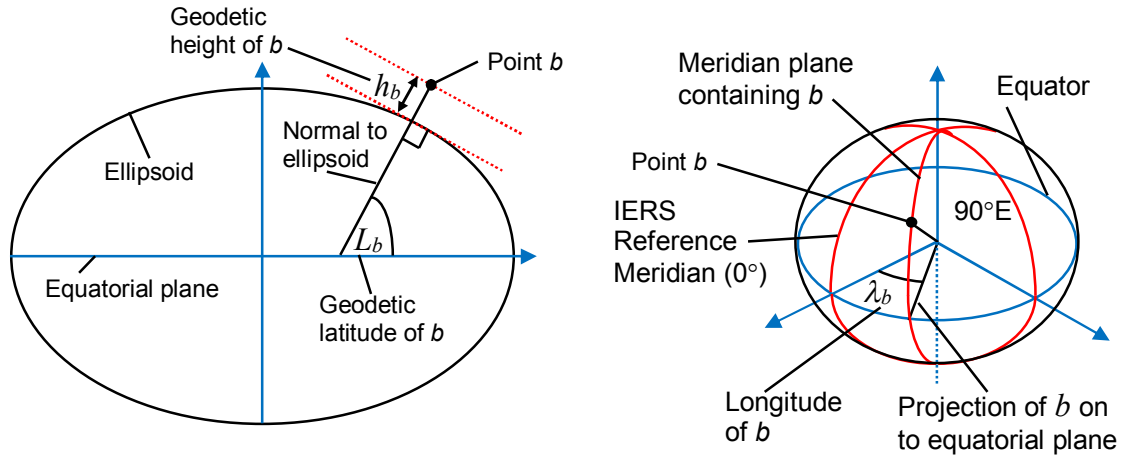noting that R_E is the transverse radius of curvature.

Figure 9. Geodetic latitude, longitude and geodetic height of point *b*

The velocity with respect to the Earth, resolved along north, east, and down (NED), an example of a local navigation frame, is obtained using [3]

$$\mathbf{v}_{eb}^n = \mathbf{C}_e^n \mathbf{C}_i^e \left(\mathbf{v}_{ib}^i - \mathbf{\Omega}_{ie}^i \mathbf{r}_{ib}^i\right), \qquad (30)$$

where

$$\mathbf{C}_e^n = \begin{pmatrix} -\sin L_b \cos \lambda_b & -\sin L_b \sin \lambda_b & \cos L_b \\ -\sin \lambda_b & \cos \lambda_b & 0 \\ -\cos L_b \cos \lambda_b & -\cos L_b \sin \lambda_b & -\sin L_b \end{pmatrix},$$

$$\mathbf{\Omega}_{ie}^i = \begin{pmatrix} 0 & -\omega_{ie} & 0 \\ \omega_{ie} & 0 & 0 \\ 0 & 0 & 0 \end{pmatrix} \qquad (31)$$

Finally, the attitude, expressed as the coordinate transformation matrix from the body frame to NED, is obtained using

$$\mathbf{C}_b^n = \mathbf{C}_e^n \mathbf{C}_i^e \mathbf{C}_b^i. \qquad (32)$$

For user output, it is more intuitive to express attitude as a set of three Euler angles. The Euler attitude of the body frame with respect to NED may be expressed as a set of three rotations from the NED to the body. Firstly, the yaw rotation, ψ_{nb}, is a

positive rotation about the z (down) axis of the NED frame. Secondly, the pitch
rotation, θ_{nb}, is a positive rotation about the y (right) axis of the first intermediate
frame. Finally, the roll rotation, ϕ_{nb}, is a positive rotation about the x (forward) axis of
the second intermediate frame. The Euler angles may be obtained from the coordinate
transformation matrix using

$$
\begin{aligned}
\phi_{nb} &= \arctan_2\left(C^n_{b3,2}, C^n_{b3,3}\right) \\
\theta_{nb} &= -\arcsin C^n_{b3,1} \qquad , \\
\psi_{nb} &= \arctan_2\left(C^n_{b2,1}, C^n_{b1,1}\right)
\end{aligned}
\tag{33}
$$

where four-quadrant arctangent functions must be used. The reverse transformation is

$$
\mathbf{C}^n_b = \mathbf{C}^{b\,\mathrm{T}}_n =
\begin{bmatrix}
\cos\theta_{nb}\cos\psi_{nb} & \begin{pmatrix} -\cos\phi_{nb}\sin\psi_{nb} \\ +\sin\phi_{nb}\sin\theta_{nb}\cos\psi_{nb} \end{pmatrix} & \begin{pmatrix} \sin\phi_{nb}\sin\psi_{nb} \\ +\cos\phi_{nb}\sin\theta_{nb}\cos\psi_{nb} \end{pmatrix} \\
\cos\theta_{nb}\sin\psi_{nb} & \begin{pmatrix} \cos\phi_{nb}\cos\psi_{nb} \\ +\sin\phi_{nb}\sin\theta_{nb}\sin\psi_{nb} \end{pmatrix} & \begin{pmatrix} -\sin\phi_{nb}\cos\psi_{nb} \\ +\cos\phi_{nb}\sin\theta_{nb}\sin\psi_{nb} \end{pmatrix} \\
-\sin\theta_{nb} & \sin\phi_{nb}\cos\theta_{nb} & \cos\phi_{nb}\cos\theta_{nb}
\end{bmatrix}
\tag{34}
$$

D. Precision North, East, Down Navigation Equations

The inertial navigation equations presented in the preceding subsection are
approximate and exhibit errors that increase with the host-vehicle dynamics, vibration
level and update interval. For most applications, a higher precision, and thus greater
complexity and processing capacity, is required. It is also common to directly compute
an Earth-referenced navigation solution resolved about north, east, and down axes (or
east, north, and up) instead of computing an ECI solution and converting. In such an
implementation it is necessary to account for the rotation of the Earth with respect to
inertial space, including the ensuing Coriolis force, and also the rotation of the NED
coordinate frame with respect to the Earth as the navigation system moves. A
derivation and explanation of the constituent terms may be found in [3, 4].

The attitude solution is updated using

$$
\mathbf{C}^n_b(+) \approx \mathbf{C}^n_b(-)\mathbf{C}^{b-}_{b+} - \left(\mathbf{\Omega}^n_{ie}(-) + \mathbf{\Omega}^n_{en}(-)\right)\mathbf{C}^n_b(-)\tau_i.
\tag{35}
$$

where, from (16), the rotation measured by the gyros is

$$
\mathbf{C}^{b-}_{b+} = \mathbf{I}_3 + \frac{\sin\left|\mathbf{\omega}^b_{ib}\tau_i\right|}{\left|\mathbf{\omega}^b_{ib}\tau_i\right|}\left[\left(\mathbf{\omega}^b_{ib}\tau_i\right)\wedge\right] + \frac{1-\cos\left|\mathbf{\omega}^b_{ib}\tau_i\right|}{\left|\mathbf{\omega}^b_{ib}\tau_i\right|^2}\left[\left(\mathbf{\omega}^b_{ib}\tau_i\right)\wedge\right]^2,
\tag{36}
$$

the skew symmetric matrix of the angular rate of the Earth, resolved about NED is

$$
\mathbf{\Omega}^n_{ie} = \omega_{ie}
\begin{pmatrix}
0 & \sin L_b & 0 \\
-\sin L_b & 0 & -\cos L_b \\
0 & \cos L_b & 0
\end{pmatrix},
\tag{37}
$$

and the skew symmetric matrix of the angular rate of the north, east, and down axes
with respect to the Earth, known as the transport rate, is

$$\boldsymbol{\Omega}_{en}^n = \begin{pmatrix} 0 & -\omega_{en,z}^n & \omega_{en,y}^n \\ \omega_{en,z}^n & 0 & -\omega_{en,x}^n \\ -\omega_{en,y}^n & \omega_{en,x}^n & 0 \end{pmatrix},$$

$$\boldsymbol{\omega}_{en}^n = \begin{pmatrix} v_{eb,E}^n \big/ (R_E(L_b) + h_b) \\ -v_{eb,N}^n \big/ (R_N(L_b) + h_b) \\ -v_{eb,E}^n \tan L_b \big/ (R_E(L_b) + h_b) \end{pmatrix}, \tag{38}$$

where

$$R_N(L_b) = \frac{R_0(1 - e^2)}{(1 - e^2 \sin^2 L_b)^{3/2}} \tag{39}$$

is the meridian radius of curvature. The attitude solution may be converted to Euler
angles using (33). The coordinate transformation matrix should also be subject to a
reorthogonalization and renormalization process at regular intervals to compensate for
computational rounding errors [3, 4].

The specific force resolving axes are transformed to NED using

$$\mathbf{f}_{ib}^n = \overline{\mathbf{C}}_b^n \mathbf{f}_{ib}^b, \qquad \overline{\mathbf{C}}_b^n = \mathbf{C}_b^n(-)\mathbf{C}_{\bar{b}}^{b-} - \tfrac{1}{2}\big(\boldsymbol{\Omega}_{ie}^n(-) + \boldsymbol{\Omega}_{en}^n(-)\big)\mathbf{C}_b^n(-)\tau_i, \tag{40}$$

where

$$\mathbf{C}_{\bar{b}}^{b-} = \mathbf{I}_3 + \frac{1 - \cos\big|\boldsymbol{\omega}_{ib}^b \tau_i\big|}{\big|\boldsymbol{\omega}_{ib}^b \tau_i\big|^2}\big[(\boldsymbol{\omega}_{ib}^b \tau_i)\wedge\big] + \frac{1}{\big|\boldsymbol{\alpha}_{ib}^b\big|^2}\left(1 - \frac{\sin\big|\boldsymbol{\omega}_{ib}^b \tau_i\big|}{\big|\boldsymbol{\omega}_{ib}^b \tau_i\big|}\right)\big[(\boldsymbol{\omega}_{ib}^b \tau_i)\wedge\big]^2. \tag{41}$$

The velocity solution is then updated using

$$\mathbf{v}_{eb}^n(+) \approx \mathbf{v}_{eb}^n(-) + \Big[\mathbf{f}_{ib}^n + \mathbf{g}_b^n(L_b(-), h_b(-)) - \big(\boldsymbol{\Omega}_{en}^n(-) + 2\boldsymbol{\Omega}_{ie}^n(-)\big)\mathbf{v}_{eb}^n(-)\Big]\tau_i, \tag{42}$$

where the acceleration due to gravity is given by [21]:

$$\begin{aligned} g_{b,D}^n(L_b, h_b) &\approx g_0(L_b)\left\{1 - \frac{2}{R_0}\left[1 + f\big(1 - 2\sin^2 L_b\big) + \frac{\omega_{ie}^2 R_0^2 R_P}{\mu}\right]h_b + \frac{3}{R_0^2}h_b^2\right\} \\ g_{b,N}^n(L_b, h_b) &\approx -8.08 \times 10^{-9} h_b \sin 2L_b \text{ m s}^{-2} \\ g_0(L_b) &\approx 9.7803253359 \frac{(1 + 0.001931853 \sin^2 L_b)}{\sqrt{1 - e^2 \sin^2 L_b}} \text{ m s}^{-2} \end{aligned}, \tag{43}$$

where $f = 1 / 298.257223563$ is the flattening of the ellipsoid.

The curvilinear position may be updated directly from the velocity using

$$\begin{aligned} h_b(+) &= h_b(-) - \frac{\tau_i}{2}\big(v_{eb,D}^n(-) + v_{eb,D}^n(+)\big) \\ L_b(+) &\approx L_b(-) + \frac{\tau_i}{2}\left(\frac{v_{eb,N}^n(-)}{R_N(L_b(-)) + h_b(-)} + \frac{v_{eb,N}^n(+)}{R_N(L_b(-)) + h_b(+)}\right) \\ \lambda_b(+) &= \lambda_b(-) + \frac{\tau_i}{2}\left(\frac{v_{eb,E}^n(-)}{(R_E(L_b(-)) + h_b(-))\cos L_b(-)} + \frac{v_{eb,E}^n(+)}{(R_E(L_b(+)) + h_b(+))\cos L_b(+)}\right) \end{aligned}, \tag{44}$$

The preceding equations should be updated at the IMU output rate. However,
it is possible to implement slower varying terms, such as the Earth rotation and
transport rate contributions, at a lower rate, reducing processor load at the expense of

increased complexity [23]. It should also be noted that a NED-resolved implementation is not suitable for use in polar regions because north and east are undefined at the poles; an ECI-frame, ECEF-frame or wander-azimuth implementation must be used instead [3, 17]. A wander-azimuth coordinate frame is a local-level frame in which the *x*- and *y*- axes are rotated about the vertical with respect to north and east by a wander angle that varies with position, avoiding the singularity at the poles.

E. INS Error Propagation

The errors in an inertial navigation solution arise from three sources: the inertial sensors, initialization errors, and processing approximations, including the gravity model. For example, the models given in (22) and (43) are accurate to about 10^{-3} m s^{-2} in each direction. These errors are integrated through the navigation equations to produce position, velocity, and attitude errors that grow with time. For example, the velocity initialization error results in a growing position error. The error propagation is also affected by the host vehicle trajectory. For example, the effect of scale factor and cross-coupling errors depends on the host vehicle dynamics, as does the coupling of the attitude errors, particularly heading, into velocity and position.

Full determination of INS error propagation is a complex problem, normally studied using simulation software. This section begins by defining the INS errors. Several examples of short-term error propagation are then presented followed by brief discussions of longer-term error propagation, the effects of maneuvers, and indexed IMUs. The Earth-referenced form of the navigation solution, resolved along north, east, and down, is used. A more detailed treatment of INS error propagation may be found in [4, 18, 20].

1) *Error Definitions.* In general, an INS error is simply the difference between an INS-indicated quantity, denoted by a "~", and the true value of that quantity. Thus, the Cartesian position, velocity and acceleration errors are

$$\delta\mathbf{r}_{eb}^{n} = \widetilde{\mathbf{r}}_{eb}^{n} - \mathbf{r}_{eb}^{n}$$
$$\delta\mathbf{v}_{eb}^{n} = \widetilde{\mathbf{v}}_{eb}^{n} - \mathbf{v}_{eb}^{n} \ . \tag{45}$$
$$\delta\mathbf{a}_{eb}^{n} = \widetilde{\mathbf{a}}_{eb}^{n} - \mathbf{a}_{eb}^{n}$$

Similarly, the latitude, longitude, and height errors are

$$\delta L_{b} = \widetilde{L}_{b} - L_{b}$$
$$\delta\lambda_{b} = \widetilde{\lambda}_{b} - \lambda_{b}$$
$$\delta h_{b} = \widetilde{h}_{b} - h_{b} \ . \tag{46}$$

As explained in Section IV.C.1, coordinate transformation matrices are multiplied to perform successive transformations or rotations. Therefore, the attitude error in coordinate transformation matrix form is obtained by multiplying the attitude solution by the transpose of the true attitude:

$$\delta\mathbf{C}_{b}^{n} = \widetilde{\mathbf{C}}_{b}^{n}\mathbf{C}_{n}^{b} \ , \tag{47}$$

noting that the attitude error components are resolved about the axes of the NED frame. Where the small angle approximation is applicable, the attitude error may also be expressed as a vector resolved about an axis of choice. For example, $\delta\boldsymbol{\psi}_{nb}^{n}$ is the

error in the INS indicated attitude of the body frame with respect to the NED frame, resolved about NED axes. This may be expressed in terms of the coordinate transformation matrix form of the attitude error using [3]

$$\left[\delta\boldsymbol{\psi}_{nb}^n \wedge\right] \approx \delta\mathbf{C}_b^n - \mathbf{I}_3 . \tag{48}$$

Finally, the specific force and angular rate errors from the accelerometer and gyro measurements are

$$\begin{aligned}\delta\mathbf{f}_{ib}^b &= \widetilde{\mathbf{f}}_{ib}^b - \mathbf{f}_{ib}^b \\ \delta\boldsymbol{\omega}_{ib}^b &= \widetilde{\boldsymbol{\omega}}_{ib}^b - \boldsymbol{\omega}_{ib}^b\end{aligned} .$$

2) *Short-Term Straight-Line Error Propagation*. As inertial navigation is most commonly integrated with GNSS and/or other sensors, short-term error propagation is of most relevance. For the short-term case, the effects of curvature and rotation of the Earth and gravity model feedback may be neglected. Here, the simplest case, in which the host vehicle is traveling in a straight line at constant velocity and remains level, is considered. Consequently, there are no dynamics-induced errors.

Figure 10 shows the position error growth with constant velocity, acceleration, attitude, and angular-rate errors. The position error is the integral of the velocity error, so with a constant velocity error,

$$\delta\mathbf{r}_{eb}^n(t) = \delta\mathbf{v}_{eb}^n t . \tag{49}$$

Thus, an 0.1 m s^{-1} initial velocity error produces a 30m position error after 300s (5 minutes).
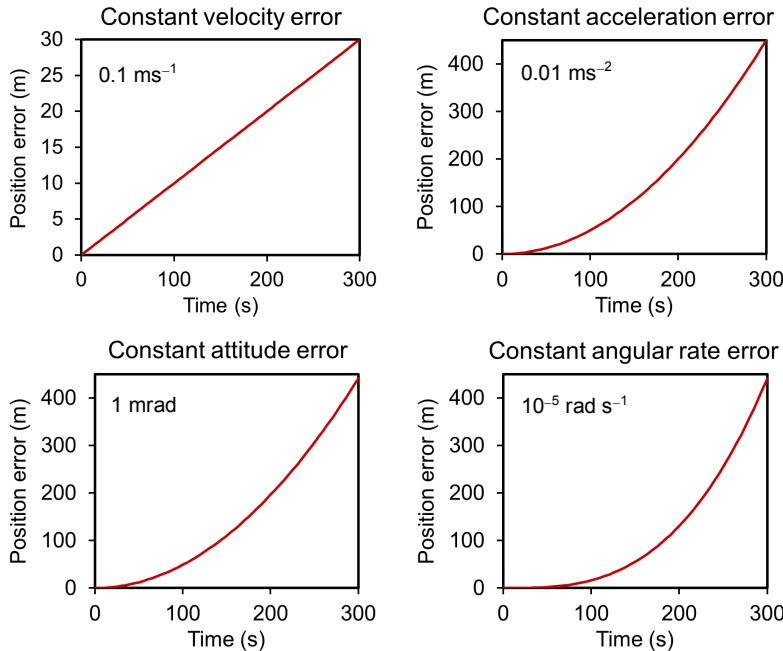

Figure 10. Short-term straight-line position error growth per axis for different error sources. (From [3] © Paul Groves 2013. Reproduced with Permission).

The velocity error is the integral of the acceleration error, so the velocity and position errors resulting from a constant accelerometer bias are:

$$\delta \mathbf{v}_{eb}^n(t) \approx \mathbf{C}_b^n \mathbf{b}_a t, \qquad \delta \mathbf{r}_{eb}^n(t) \approx \tfrac{1}{2} \mathbf{C}_b^n \mathbf{b}_a t^2 , \tag{50}$$

and an 0.01 m s^{-2} ($\sim$ 1 mg) accelerometer bias produces a 450m position error after 300s. Acceleration errors can also result from gravity modeling approximations. For example, the models in Sections IV.C.3 and IV.D are typically accurate to about 10^{-3} m s^{-2} (0.1 mg) in each direction [4, 20].

Attitude errors produce errors in the transformation of the specific-force resolving axes from the body frame to the NED frame, resulting in errors in the acceleration resolved in that frame. Figure 11 illustrates this. Where the attitude error may be expressed as a small angle, the resulting acceleration error is

$$\delta \mathbf{a}_{eb}^n(t) \approx \delta \boldsymbol{\psi}_{nb}^n \wedge \left(\mathbf{C}_b^n \widetilde{\mathbf{f}}_{ib}^b \right). \tag{51}$$
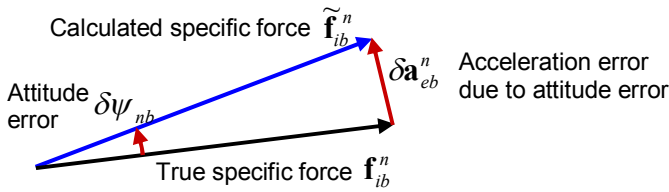

Figure 11. Acceleration error due to attitude error. (From [3] © Paul Groves 2013. Reproduced with Permission).

In the constant-velocity and level example, the specific force comprises only the reaction to gravity. Thus, pitch (body-frame *y*-axis) attitude errors couple into along-track (body-frame *x*-axis) acceleration errors and roll (body-frame *x*-axis) attitude errors couple into across-track (body-frame *y*-axis) acceleration errors. These acceleration errors are integrated to produce the following velocity and position errors.

$$\delta \mathbf{v}_{eb}^n(t) \approx \delta \boldsymbol{\psi}_{nb}^n \wedge \begin{pmatrix} 0 \\ 0 \\ -g \end{pmatrix} t, \qquad \delta \mathbf{r}_{eb}^n(t) \approx \tfrac{1}{2} \delta \boldsymbol{\psi}_{nb}^n \wedge \begin{pmatrix} 0 \\ 0 \\ -g \end{pmatrix} t^2 . \tag{52}$$

A 1 mrad (0.057°) initial attitude error therefore leads to a position error of $\sim$440m after 300s.

Similarly, the velocity and position errors due to the gyro bias are

$$\delta \mathbf{v}_{eb}^n(t) \approx \tfrac{1}{2} \left(\mathbf{C}_b^n \mathbf{b}_g \right) \wedge \begin{pmatrix} 0 \\ 0 \\ -g \end{pmatrix} t^2, \qquad \delta \mathbf{r}_{eb}^n(t) \approx \tfrac{1}{6} \left(\mathbf{C}_b^n \mathbf{b}_g \right) \wedge \begin{pmatrix} 0 \\ 0 \\ -g \end{pmatrix} t^3 , \tag{53}$$

while a 10^{-5} rad s^{-1} (2.1 ° hr^{-1}) gyro bias produces a $\sim$439m position error after 300s.

The other major source of error in this scenario is inertial sensor noise, which may be considered white over timescales exceeding one second. If the single-sided accelerometer noise PSD is S_a, the standard deviations of the ensuing velocity and position errors are

$$\begin{aligned} \sigma\left(\delta v_{eb,i}^n \right) &= \sqrt{S_a t} \qquad i \in N, E, D \\ \sigma\left(\delta r_{eb,i}^n \right) &= \sqrt{\tfrac{1}{3} S_a t^3} \end{aligned} . \tag{54}$$

Similarly, if the gyro noise PSDs is S_g, the standard deviations of the ensuing attitude errors and horizontal position and velocity errors are

$$\sigma\left(\delta\psi_{nb,i}^n\right)=\sqrt{S_g t} \qquad i\in N,E,D$$
$$\sigma\left(\delta v_{eb,j}^n\right)=g\sqrt{\tfrac{1}{3}S_g t^3} \qquad j\in N,E \qquad .$$
$$\sigma\left(\delta r_{eb,j}^n\right)=g\sqrt{\tfrac{1}{5}S_g t^5}$$

(55)

Figure 12 shows the growth in position error standard deviation due to sensor noise. If the accelerometer random noise PSD is 10^{-6} m^2 s^{-3} (corresponding to a root PSD of about 100 μg/√Hz), the position error standard deviation after 300s is 3m per axis. Similarly, if the gyro random noise PSD is 10^{-9} rad^2 s^{-1} (a root PSD of ~0.1 °/√hr), the position error standard deviation after 300s is ~22m per horizontal axis.
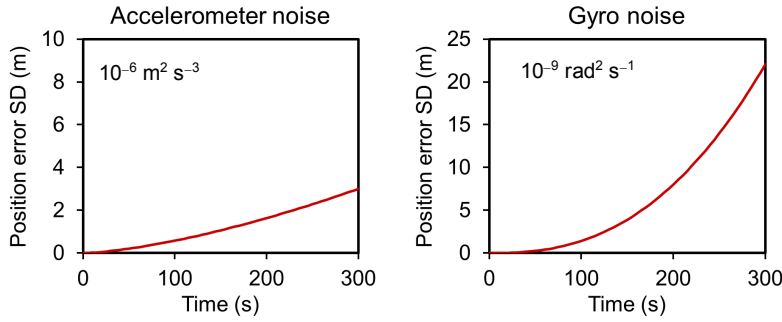

Figure 12. Short-term straight-line position error standard deviation growth per axis due to inertial sensor noise. (From [3] © Paul Groves 2013. Reproduced with Permission).

Figure 13 shows the growth of the horizontal position error standard deviation using tactical-grade and aviation-grade INSs with the characteristics listed in Table 2. The tactical-grade INS error is more than an order of magnitude bigger than that of the aviation-grade INS after 300s. The difference in horizontal and vertical performance of the tactical-grade INS arises because the gyro bias dominates and, under constant velocity conditions, this only affects horizontal navigation. For the aviation-grade INS, the acceleration, roll, and pitch errors dominate. The initial position error has little impact after the first minute. Where a tactical-grade INS is calibrated through sensor integration or fine alignment (Section VI), the errors are reduced by about a factor of 10.
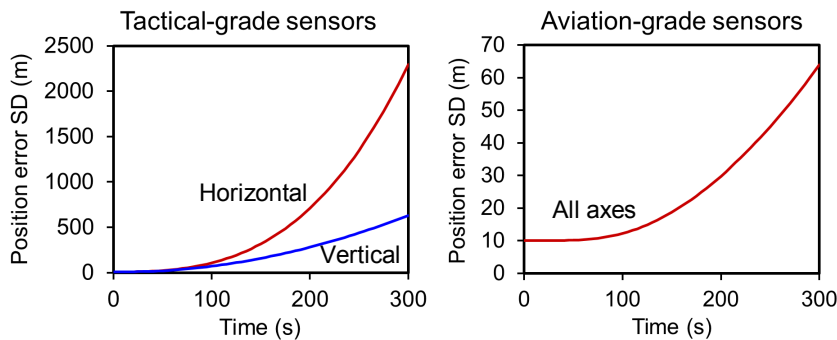

Figure 13 Short-term straight-line position error standard deviation growth per axis for tactical-grade and aviation-grade INSs. (From [3] © Paul Groves 2013. Reproduced with Permission).

Table 2. Tactical-grade and Aviation-grade INS Characteristics

Sensor grade	Tactical	Aviation
Initial position error SD	10m	10m
Initial velocity error SD	0.1 m s^{-1}	0.01 m s^{-1}
Initial (roll and pitch) attitude error SD	1 mrad	0.1 mrad
Accelerometer bias SD	0.01 m s^{-2} (1 mg)	0.001 m s^{-2} (0.1 mg)
Gyro bias SD	5×10^{-5} rad s^{-1} (10 ° hr^{-1})	5×10^{-8} rad s^{-1} (0.01 ° hr^{-1})
Accelerometer noise PSD	10^{-6} m^2 s^{-3} (100 °g/√Hz)^2	10^{-7} m^2 s^{-3} (32 °g/√Hz)^2
Gyro noise PSD	10^{-9} rad^2 s^{-1} (0.1 °/√hr)^2	10^{-12} rad^2 s^{-1} (0.003 °/√hr)^2

3) *Longer-Term Error Propagation.* Longer term INS error propagation is affected by the gravity model. A horizontal position error results in the gravity model assuming that gravity acts at an angle to its true direction, producing a horizontal acceleration error. However, this acceleration error is in the opposite direction to the position error, providing negative feedback and correcting the error. Consequently, the position error due to a velocity, attitude, or acceleration error undergoes a bounded simple harmonic oscillation, known as Schuler oscillation, with a period of approximately 84 minutes. The position error due to an angular rate error comprises the sum of a linearly growing term and an oscillatory term. Thus, over the long term, it is the quality of the gyros that determines the overall accuracy of an inertial navigation system. Further details may be found in [3, 4, 20].

A positive height error causes the magnitude of the gravity to be underestimated, resulting in a positive vertical acceleration error. Thus, in the vertical direction, there is positive feedback through the gravity model and the solution is unstable. Historically, aircraft INS have been integrated with barometric altimeters to stabilize the vertical channel. Today, this stabilization may also be achieved through integration with GNSS. For land and sea applications, a motion constraint may be used.

4) *Maneuver-Dependent Errors.* Much of the error propagation in inertial navigation is dependent on the host vehicle maneuvers. As explained in Section IV.E.2, the effect of attitude errors on the velocity and position solutions depends on the specific force. The heading error only has an impact during maneuvers. A linear acceleration or deceleration maneuver couples the heading error into the cross-track velocity and the pitch error into the vertical velocity. A turn produces transverse acceleration, which couples the heading error into the along-track velocity and the roll error into the vertical velocity.

The heading error is typically an order of magnitude larger than the roll and pitch errors because it is more difficult to initialize and calibrate. Consequently, significant maneuvers can lead to rapid changes in velocity error. Figure 14 shows the velocity errors of an aircraft, initially flying north at 100 m s^{-1} with north and east velocity errors of 0.05 m s^{-1} and 0.1 m s^{-1}, respectively, and a heading error of 1

mrad. The aircraft then accelerates to 200 m s⁻¹, resulting in the east velocity error
doubling to 0.2 m s⁻¹. Later, it undergoes a 90° turn to the west at constant speed,
which increases the north velocity error to 0.25 m s⁻¹ and drops the east velocity error
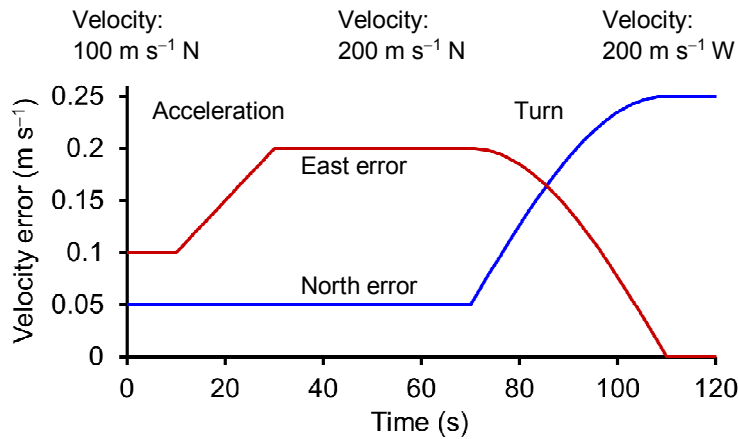to zero.

Figure 14. Illustration of the effect of maneuver on velocity error with a 1 mrad
heading error. (From [3] © Paul Groves 2013. Reproduced with Permission).

The effect of scale factor and cross-coupling errors, gyro g-dependent errors,
and higher-order inertial sensor errors on navigation error growth also depends on the
maneuvers. In the previous example, a 500 ppm *x*-accelerometer scale factor error
would produce an increase in north velocity error during the acceleration maneuver of
0.05 m s⁻¹, while a *z*-gyro scale factor error of –637 ppm would double the heading
error to 2 mrad during the turn.

Velocity and direction changes often cancel out over successive maneuvers, so
the effects of the scale factor and cross-coupling errors largely average out. An
exception is circular and oval trajectories where the gyro scale factor and cross-
coupling errors produce attitude errors that grow with time. Using tactical-grade gyros
with scale factor and cross-coupling errors of around 300 ppm, the attitude errors will
increase by about 0.1° per axis for each circuit completed by the host vehicle. With a
circling period of 2 minutes, the position error will increase by about 400m per hour.

With a figure-of-eight trajectory, the attitude error due to gyro scale factor and
cross-coupling errors will be oscillatory and correlated with the direction of travel.
This produces a velocity error that increases with each circuit. Using tactical-grade
gyros, position errors of several kilometers can build up over an hour.

INS error propagation is also affected by vibration. Synchronized angular
oscillation about two orthogonal axes, known as coning, results in a constant angular
rate error. Similarly, linear oscillation synchronized with angular oscillation about an
orthogonal axis, known as sculling results in a constant acceleration error. These
coning and sculling errors are larger when the update interval is larger and/or there are
approximations in the navigation equations [3, 4].

5) *Indexed IMUs.* In an *indexed* or *carouseling* IMU, the inertial sensor
assembly is regularly rotated with respect to the casing, usually in increments of 90°.
This enables the cancellation over time of the position and velocity errors due to the

accelerometer and gyro biases. From (50) and (53), the growth in the position and velocity errors depends on the attitude. Therefore, if the direction of an inertial sensor's sensitive axis is regularly reversed, its bias will lead to oscillatory position and velocity errors instead of continuously growing errors. To achieve this, it is rather more convenient to turn the inertial sensor assembly than to turn the entire host vehicle.

Single-axis indexing normally employs rotation of the inertial sensor assembly about the z-axis, generally the vertical. This enables cancellation of the effects of x- and y-axis accelerometer and gyro biases, but not the z-axis biases. The z-axis gyro bias has less impact on navigation accuracy as maneuvers are needed to couple the heading error into the position and velocity errors, while the z-axis accelerometer bias mainly affects vertical positioning which always requires aiding from another sensor or a motion constraint. Dual-axis indexing enables cancellation of the effects of all six sensor biases on horizontal positioning [24]. These systems are designed so that the errors induced by the sensor rotations cancel out over the course of a rotation cycle.

V. ATTITUDE DETERMINATION

This section describes how inertial sensors may be used for absolute attitude determination, both on their own and with magnetometers. Accelerometer leveling, gyrocompassing, magnetic heading determination, and the attitude and heading reference system (AHRS) are described in turn.

A. Accelerometer Leveling

When an INS is stationary, the only specific force sensed by the accelerometers is the reaction to gravity. The specific force measurements are resolved along body-frame axes, whereas predictions from a gravity model are resolved along north, east, and down. Therefore from (2) and (11), the attitude, $\mathbf{C}_b^n$, can be estimated by solving

$$\mathbf{f}_{ib}^b = -\mathbf{C}_n^b \mathbf{g}_b^n (L_b, h_b),$$ (56)

given that $\mathbf{a}_{eb}^n = 0$. At the Earth's surface, the reaction to gravity is in the up direction of a local navigation frame. Therefore, neglecting the first two components of $\mathbf{g}_b^n$ and replacing the third column of $\mathbf{C}_n^b$ with the corresponding Euler angles, obtained from (34), gives

$$\begin{pmatrix} f_{ib,x}^b \\ f_{ib,y}^b \\ f_{ib,z}^b \end{pmatrix} = \begin{pmatrix} \sin\theta_{nb} \\ -\cos\theta_{nb}\sin\phi_{nb} \\ -\cos\theta_{nb}\cos\phi_{nb} \end{pmatrix} g_{b,D}^n (L_b, h_b),$$ (57)

where θ_{nb} is pitch, ϕ_{nb} is roll, and $g_{b,D}^n$ is the down component of the acceleration due to gravity. This solution is overdetermined. Therefore, gravity can be eliminated to give

$$\theta_{nb} = \arctan\left(\frac{f_{ib,x}^b}{\sqrt{f_{ib,y}^b{}^2 + f_{ib,z}^b{}^2}} \right), \qquad \phi_{nb} = \arctan_2\left(-f_{ib,y}^b, -f_{ib,z}^b \right),$$ (58)

noting that a four-quadrant arctangent function must be used for roll. Heading cannot be determined by leveling because the orientation of the gravity vector within the body frame is independent of it.

Where the INS is absolutely stationary, the accuracy is determined only by the accelerometer errors. For example, a 1 mrad roll and pitch accuracy is obtained from accelerometers accurate to 10^{-3} g. Disturbing motion, such as mechanical vibration, wind effects, and human activity, disrupts the leveling process. However, if the motion averages out over time, its effects may be mitigated simply by time-averaging the accelerometer measurements over a few seconds.

Leveling should not be performed when the host vehicle is maneuvering and attempting to do so can lead to large errors. Therefore, accelerometer leveling measurements should only be accepted when $\left|\mathbf{f}_{ib}^{b}\right| \approx \left|\mathbf{g}_{b}^{n}\right|$.

B. Gyrocompassing

When the INS is stationary, the only rotation it senses is that of the Earth, which is about the z direction of an ECEF frame. Measuring this rotation in the body frame enables the heading to be determined, except close to the poles, where the rotation axis and gravity vector coincide. There are two types of gyrocompassing, direct and indirect.

Direct gyrocompassing measures the Earth rotation directly using the gyros. The attitude, $\mathbf{C}_{b}^{n}$, may be obtained by solving

$$\boldsymbol{\omega}_{ib}^{b} = \mathbf{C}_{n}^{b}\mathbf{C}_{e}^{n}(L_{b}, \lambda_{b})\begin{pmatrix} 0 \\ 0 \\ \omega_{ie} \end{pmatrix}, \tag{59}$$

given that $\boldsymbol{\omega}_{eb}^{n} = 0$. Substituting in (31) and rearranging,

$$\begin{pmatrix} \cos L_{b}\omega_{ie} \\ 0 \\ -\sin L_{b}\omega_{ie} \end{pmatrix} = \mathbf{C}_{b}^{n}\boldsymbol{\omega}_{ib}^{b}, \tag{60}$$

Solving the middle row of (60), substituting the corresponding Euler angles into $\mathbf{C}_{b}^{n}$, enables the heading to determined without knowledge of position, provided the roll and pitch are known (e.g., from leveling):

$$\begin{aligned} \psi_{nb} &= \arctan_{2}\left(\sin\psi_{nb}, \cos\psi_{nb}\right) \\ \sin\psi_{nb} &= -\omega_{ib,y}^{b}\cos\phi_{nb} + \omega_{ib,z}^{b}\sin\phi_{nb} \\ \cos\psi_{nb} &= \omega_{ib,x}^{b}\cos\theta_{nb} + \omega_{ib,y}^{b}\sin\phi_{nb}\sin\theta_{nb} + \omega_{ib,z}^{b}\cos\phi_{nb}\sin\theta_{nb} \end{aligned} \tag{61}$$

Again, a four-quadrant arctangent function must be used. Leveling and direct gyrocompassing may also be performed in one step where the latitude is known [4].

If there is any disturbing motion, the gyro measurements must be time averaged. However, even small levels of angular vibration will be much larger than the Earth-rotation rate. Therefore, if the INS is mounted on any kind of vehicle, an averaging time of many hours can be required. Consequently, the application of direct gyrocompassing is limited.

Indirect gyrocompassing uses the gyros to compute a relative attitude solution, which is used to transform the specific-force measurements into inertial resolving

axes. The direction of the Earth's rotation is then obtained from rotation of the inertially resolved gravity vector about this axis as shown in Figure 15. Indirect gyrocompassing typically takes 2 to 10 minutes, depending on the amount of vibration and disturbance and the accuracy required. Suitable quasi-stationary alignment algorithms are described in [3, 18, 25].
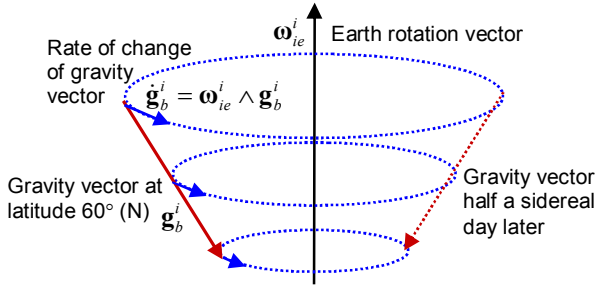

Figure 15. Earth rotation and gravity vectors resolved in ECI-frame axes. (From [3] © Paul Groves 2013. Reproduced with Permission).

The accuracy achievable using gyrocompassing depends on gyro performance. Given that $\omega_{ie} \approx 7\times10^{-5}$ rad s^{-1}, to obtain a 1 mrad heading initialization at the equator, the gyros must be accurate to around 7×10^{-8} rad s^{-1} (0.01 ° hr^{-1}). Only aviation- and marine-grade gyros are this accurate.

C. Magnetic Heading

A three-axis magnetic compass measures the magnitude and direction of the Earth's magnetic field using a triad of magnetometers with mutually perpendicular sensitive axes. Fluxgate magnetometers, magnetoinductive sensors, and magnetoresistive sensors are all suitable [26]. Accelerometer leveling or an inertial attitude solution is used to determine the pitch and roll. This enables the heading of the unit with respect to the direction of the Earth's magnetic field, known as magnetic north, to be determined using

$$\widetilde{\psi}_{mb} = \arctan_2 \begin{pmatrix} -\widetilde{m}^b_{m,y}\cos\hat{\phi}_{nb} + \widetilde{m}^b_{m,z}\sin\hat{\phi}_{nb}, \\ \widetilde{m}^b_{m,x}\cos\hat{\theta}_{nb} + \widetilde{m}^b_{m,y}\sin\hat{\phi}_{nb}\sin\hat{\theta}_{nb} + \widetilde{m}^b_{m,z}\cos\hat{\phi}_{nb}\sin\hat{\theta}_{nb} \end{pmatrix}, \tag{62}$$

where $\widetilde{\mathbf{m}}^b_m$ is the measured magnetic flux density and a four-quadrant arctangent function must be used.

The heading with respect to true north is then given by

$$\widetilde{\psi}_{nb} = \widetilde{\psi}_{mb} + \alpha_{nE}, \tag{63}$$

where α_{nE} is the declination angle or magnetic variation of the Earth's magnetic field. This is the bearing of the magnetic field from true north and varies predictably with both position and time. Global models, such as the International Geomagnetic Reference Field (IGRF) and the US/UK World Magnetic Model (WMM), are updated every five years. They are typically accurate to about 0.5°, but can exhibit errors of several degrees in places [26]. Higher resolution national models are available for some countries.

Further errors arise due to magnetic fields from other sources. Land applications are affected by man-made objects, such as vehicles, buildings, bridges,

lamp posts, and power lines [27, 28]. These fields can be significant several meters away and cannot easily be distinguished from the Earth's magnetic field. These local anomalies may be detected by comparing the magnitude of the measured magnetic flux density with that of the Earth's magnetic field, enabling inconsistent measurements to be rejected. This may be enhanced by also comparing orientation of the magnetic field with respect to the vertical [29]. However, heading errors of several degrees can remain undetected, while out-of-date heading measurements must be used when an anomaly is detected. Better performance is thus obtained if the magnetic heading is also smoothed using another sensor, such as gyroscopes.

As well as the geomagnetic field and local anomalies, the magnetometers also measure the magnetic field of the navigation system itself, the host vehicle, and any equipment carried. This comprises a mixture of hard-iron and soft-iron magnetism. Hard-iron magnetism is simply the magnetic fields produced by permanent magnets and electrical equipment. It is usually a few percent of the Earth's magnetic field, but can sometimes exceed it. Soft-iron magnetism is produced by materials that distort the underlying magnetic field. It is typically largest in ships, where it can distort the magnetic field by about 10%.

As the equipment magnetism moves with the magnetic compass, it can be calibrated using a process known as *swinging*, whereby a series of measurements are taken with the instrument at different orientations at a fixed location, varying the roll and pitch as well as the heading [30, 31].

D. Attitude and Heading Reference System

Figure 16 depicts an attitude and heading reference system, which comprises a low-cost IMU with consumer- or tactical-grade sensors and a magnetic compass. It is typically used for low-cost aviation applications [32], such as private aircraft and UAVs, and provides a three-component inertial attitude solution without position and velocity. For marine applications, it is sometimes known as a strapdown gyrocompass.
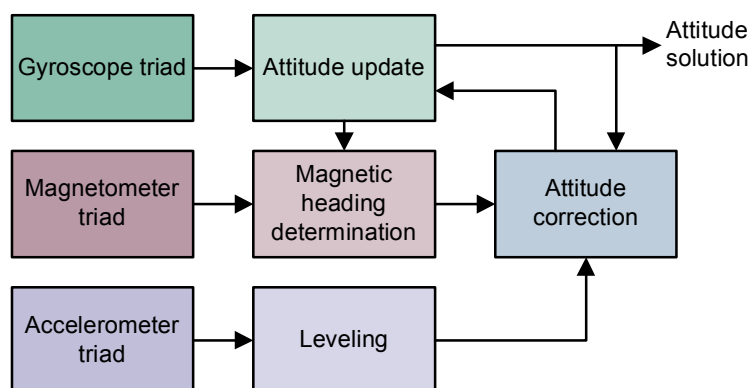

Figure 16. Basic schematic of an attitude and heading reference system. (From [3] © Paul Groves 2013. Reproduced with Permission).

The attitude is maintained by integrating the gyro measurements. The accelerometers measure roll and pitch by leveling (Section V.A), which is used to correct the gyro-derived pitch. Similarly, the magnetic compass (Section V.C) is used

to correct the gyro-derived heading. This may be accomplished using a simple
smoothing filter:

$$\hat{\phi}_{nb}(t) = W_l\hat{\phi}_{nb,l}(t) + (1 - W_l)\left[\hat{\phi}_{nb}(t - \tau) + \dot{\phi}_{nb}\tau\right]$$
$$\hat{\theta}_{nb}(t) = W_l\hat{\theta}_{nb,l}(t) + (1 - W_l)\left[\hat{\theta}_{nb}(t - \tau) + \dot{\theta}_{nb}\tau\right] \quad , \tag{64}$$
$$\hat{\psi}_{nb}(t) = W_m\hat{\psi}_{nb,m}(t) + (1 - W_m)\left[\hat{\psi}_{nb}(t - \tau) + \dot{\psi}_{nb}\tau\right]$$

where t is time; τ is the time interval; $\hat{\phi}_{nb}$, $\hat{\theta}_{nb}$, and $\hat{\psi}_{nb}$ is the roll, pitch, and yaw

solution; $\hat{\phi}_{nb,l}$ and $\hat{\theta}_{nb,l}$ are the roll and pitch measurements from leveling; $\hat{\psi}_{nb,m}$ is the

heading obtained from the magnetic compass; W_l is the leveling weighting; W_m is the
magnetometer weighting; and $\dot{\phi}_{nb}$, $\dot{\theta}_{nb}$, and $\dot{\psi}_{nb}$ are the roll rate, pitch rate, and yaw
rate derived from the gyro measurements using

$$\begin{pmatrix} \dot{\phi}_{nb} \\ \dot{\theta}_{nb} \\ \dot{\psi}_{nb} \end{pmatrix} \approx \begin{pmatrix} 1 & \sin\hat{\phi}_{nb}\tan\hat{\theta}_{nb} & \cos\hat{\phi}_{nb}\tan\hat{\theta}_{nb} \\ 0 & \cos\hat{\phi}_{nb} & -\sin\hat{\phi}_{nb} \\ 0 & \sin\hat{\phi}_{nb}/\cos\hat{\theta}_{nb} & \cos\hat{\phi}_{nb}/\cos\hat{\theta}_{nb} \end{pmatrix}\boldsymbol{\omega}_{ib}^b, \tag{65}$$

noting that the Earth-rotation and transport-rate (see Section IV.D) must be neglected
where position and velocity are unknown.

More sophisticated AHRS use a Kalman filter (Section VI) to perform the
attitude integration. In either case, the weighting of the leveling measurements is
normally reduced or zeroed when host-vehicle maneuvers are detected. Similarly, the
magnetic heading measurements may be down-weighted or rejected when magnetic
anomalies are detected.

Performance depends on the quality of the inertial sensors and the type of
processing used. A typical AHRS provides roll and pitch to a 10-mrad (0.6°) accuracy
and heading to a 20-mrad (1.2°) accuracy, but this may be degraded by a factor of 2
during high-dynamic maneuvers.

VI. INTEGRATION AND ALIGNMENT

As explained in Section IV.E, the error in the position, velocity, and attitude
solution of an inertial navigation system normally grows with time, primarily due to
IMU measurement errors, but also due to initialization errors and approximations in
the navigation equations. This error growth may be minimized by using a series of
position and/or velocity aiding measurements from another source. This is known as
integration where the measurements are provided continually and *alignment* where
they are only available during the initialization process. In some systems, attitude
measurements are also provided. However, where there is sufficient maneuvering, the
attitude errors may be inferred from position and velocity measurements. The inertial
sensor errors may also be calibrated.

Inertial navigation may be integrated with many different navigation
technologies [3, 19]. INS is most commonly integrated with global navigation satellite
systems (GNSS), such as the Global Positioning System (GPS). GNSS computes a
position solution from measurements of the time taken for radio signals to propagate
from a constellation of orbiting satellites [33, 34]. Unlike an inertial navigation
solution, the GNSS position solution does not normally degrade with time.

For indoor navigation, inertial navigation may be integrated with positioning systems using other radio signals, such as Wi-Fi and ultra-wideband (UWB), while, for underwater applications, acoustic ranging is typically used. Position information may also be inferred from cameras, laser scanners, radar, and sonar. For land applications, position corrections may be obtained from map matching on the basis that road vehicles normally travel on roads, trains stay on tracks, and pedestrians don't walk through walls. In multisensor integrated navigation systems, a variety of different navigation and positioning technologies are combined [3, 19]. This may include additional dead-reckoning technologies, such as odometry (wheel speed), Doppler radar, or Doppler sonar. Sources of attitude information include magnetometers (Section V.C), cameras, and multi-antenna GNSS.

An important question is why inertial navigation is used at all when a drift-free position and velocity solution is available from another source. There are several reasons. Firstly, an INS typically exhibits less short-term noise than technologies, such as GNSS, that measure position directly, so the integrated solution is smoother and more accurate. Secondly, an INS provides a much higher bandwidth, with an update rate of at least 50 Hz and lower latency than many other sensors. Thirdly, attitude, acceleration, and angular rate are provided in addition to position and velocity. Finally, INS integration enables a continuous navigation solution to be maintained, whereas position-fixing technologies fail when insufficient signals are received or landmarks observed. For example, GNSS signals are highly vulnerable to incidental and deliberate interference, and can be blocked by buildings and mountainous terrain.

Alignment algorithms may use the same sources of aiding measurements as integration algorithms. In addition, transfer alignment uses velocity, and sometimes attitude, measurements from another INS or integrated INS/GNSS aboard the same host vehicle, while quasi-stationary alignment derives aiding measurements from knowledge that the INS is approximately stationary with respect to the Earth [3, 18, 25].

Figure 17 shows the basic configuration of a typical integrated navigation system. The integration algorithm, usually based on a Kalman filter, compares the inertial navigation solution with the outputs of an aiding system, such as GNSS, and estimates corrections to the inertial position, velocity, and attitude solution, usually alongside other parameters. The corrected inertial navigation solution then forms the integrated navigation solution, noting that closed loop correction is shown in Figure 17. This architecture ensures that an integrated navigation solution is always produced, regardless of the availability of aiding measurements. A detailed discussion of integration architectures may be found in [3]. Figure 18 shows the typical stages of an integration or alignment algorithm.
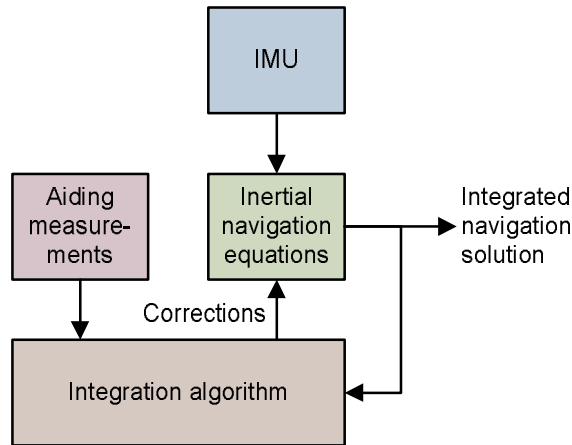
Figure 17. Generic integration architecture [3].
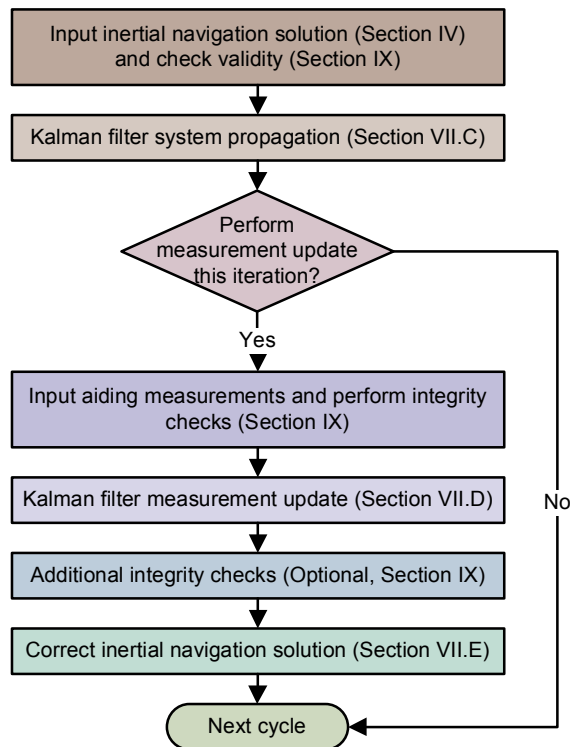
Figure 18. Typical stages of an integration or alignment algorithm [3].

The rest of this section comprises an introduction to the Kalman filter, a
discussion of state selection, the system propagation, and measurement update, and
the correction of the navigation solution.

A. Introduction to the Kalman Filter
The Kalman filter is an estimation algorithm that maintains real-time estimates
of a number of parameters of a system, such as its position and velocity, which may
continually change. The estimates are updated using a stream of measurements that
are subject to noise. The measurements must be functions of the parameters estimated,

but the set of measurements at a given time need not contain sufficient information to uniquely determine the values of the parameters at that time.

The Kalman filter uses knowledge of the deterministic and statistical properties of the system parameters and the measurements to obtain optimal estimates given the information available. It is a Bayesian estimation technique. It is supplied with an initial set of estimates and then operates recursively, updating its working estimates as a weighted average of their previous values and new values derived from the latest measurement data.

A Kalman filter has five core elements: the state vector and covariance, the system model, the measurement vector and covariance, the measurement model, and the algorithm.

The state vector, $\mathbf{x}$, is the set of parameters describing a system, known as states, which the Kalman filter estimates. For integration and alignment of inertial navigation systems, the states include the position error, velocity error, and attitude error. Associated with the state vector is an error covariance matrix, $\mathbf{P}$. This represents the uncertainties in the Kalman filter's state estimates and the degree of correlation between the errors in those estimates. This correlation information may be used to infer one state from another. Thus, the velocity error could be estimated from the rate of change of the position error. Similarly, the attitude an acceleration errors may be inferred from the variation of the velocity error.

The system model, also known as the process model or time-propagation model, describes the known variation of the Kalman filter states over time. For example, the position error varies with time as the integral of the velocity error. This is expressed using the transition matrix, $\mathbf{\Phi}$, which relates the value of the state vector at the previous epoch in time to its current value. The transition matrix is also used to update the state error covariance matrix. However, the state uncertainties must also be increased with time to account for unknown changes in the system, such as random noise on an instrument output. This variation in the true values of the states is known as system noise or process noise, and is described by the system noise covariance matrix, $\mathbf{Q}$.

The measurement vector, $\mathbf{z}$, is a set of simultaneous measurements of properties of the system which are functions of the state vector, such as the difference in navigation solution between an INS under calibration and a reference navigation system. This is the information from which all of the state estimates are derived after initialization. Associated with the measurement vector is a measurement noise covariance matrix, $\mathbf{R}$, which describes the statistics of the noise on the measurements.

The measurement model describes how the measurements vary as a function of the states. For example, the difference in velocity measurements between an INS and a reference system is directly proportional to the INS velocity error. In a linear Kalman filter, the measurement model is

$$\mathbf{z} = \mathbf{Hx} + \mathbf{w}_m \, , \tag{66}$$

where $\mathbf{H}$ is the measurement matrix and $\mathbf{w}_m$ is the measurement noise vector. The measurement model also enables the Kalman filter to compare the measurement noise covariance, $\mathbf{R}$, with the state error covariance, $\mathbf{P}$, to determine the optimal weighting of the new measurements.

The Kalman filter algorithm uses the measurement vector, measurement model, and system model to maintain optimal estimates of the state vector. It consists

of two phases, system propagation and measurement update, which together comprise up to 10 steps per iteration. These are shown in Figure 19. Steps 1–4 form the system-propagation phase and steps 5–10 the measurement-update phase. Clear introductions to Kalman filter-based estimation, suitable for beginners, may be found in [35, 36], while more comprehensive coverage is presented in [37, 38], and its application to integrated navigation is described in detail in [3, 10, 19]. Here, a relatively simple example is presented.
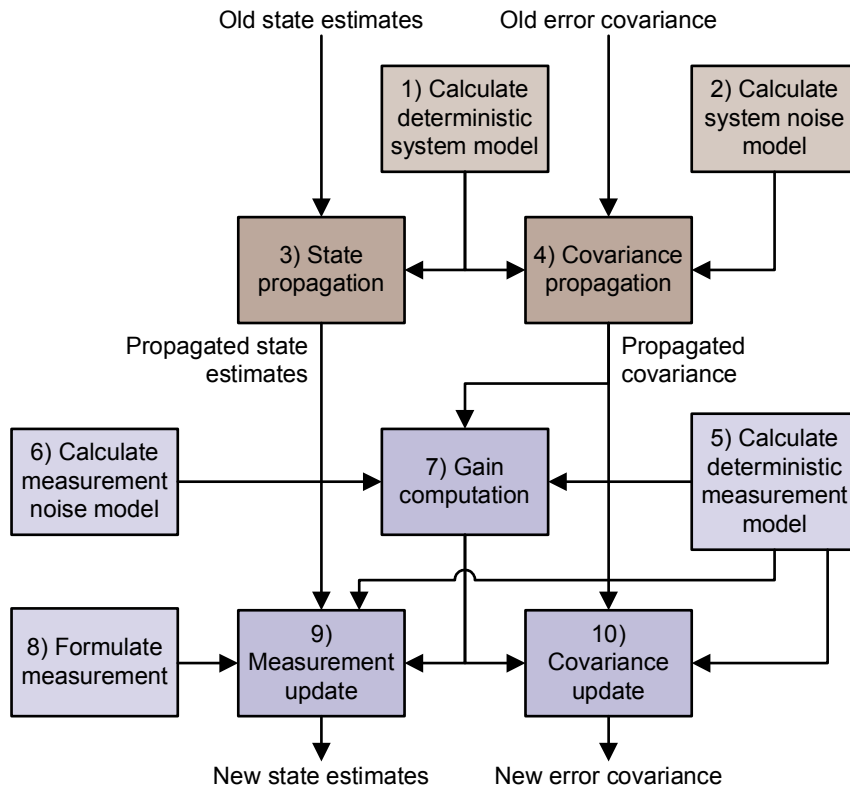

Figure 19. Kalman filter algorithm steps. (From [3] © Paul Groves 2013. Reproduced with Permission).

B. State Selection

Most INS integration and alignment algorithms implement an error-state Kalman filter (or derivative thereof), where the states estimated comprise a selection of the INS errors, defined in Section IV.E.1. The position and velocity errors are always estimated. For all but the highest grades of INS, there is significant benefit in estimating the attitude error which, here, is expressed in the small angle form.

The choice of inertial instrument errors (Section III) to estimate depends on how they affect the position, velocity, and attitude solution. If an IMU error has a significant impact on the navigation accuracy, it will be observable. Conversely, if its impact is much less than that of the random noise, which cannot be calibrated, it will not be observable. In practice, this depends on the user dynamics and the IMU design.

The following discussion assumes that position and/or velocity measurements are available from an aiding source, but not attitude measurements. The attitude errors are therefore observed through the variation in the velocity error they produce.

Except where they are very small, the accelerometer biases should always be estimated where the attitude errors are estimated. Conversely, the attitude errors should always be estimated where the accelerometer biases are estimated. Otherwise, the attitude error estimates are contaminated by the effects of the acceleration errors or vice versa. This is because both types of error lead to a linear growth in velocity error and quadratic growth in position error (see Section IV.E).

As (51) shows, acceleration errors arise where the specific force is perpendicular to the rotation axis of the attitude error. Thus, the heading error only produces a velocity error when there is acceleration in the horizontal plane. Therefore, the navigation system's host must undergo significant maneuvering for the INS heading error to be observed and calibrated. When the navigation system is level and not accelerating, the vertical accelerometer bias is the only Kalman filter state that causes growth of the vertical velocity error. This makes it the most observable of the accelerometer biases, so vertical navigation is normally better than horizontal during periods of a few minutes without aiding measurements. The roll and pitch attitude errors and horizontal accelerometer biases are observed as linear combinations under conditions of constant acceleration and attitude. To fully separate the estimates of these states, the host-vehicle must turn, while a period of forward acceleration enables separation of the pitch error and forward accelerometer bias.

The gyro biases are also estimated in most integration and alignment algorithms. These are the only significant error sources that produce a quadratic growth in the velocity error with time.

Whether it is worth estimating the accelerometer and gyro scale factor and cross-coupling errors or the gyro g-dependent biases depends on the size of the errors and the behavior of the host vehicle (see Section IV.E.3). These errors have most impact in highly dynamic applications, such as motor sports, combat aircraft, and some guided weapons. Gyro scale factor and cross-coupling errors can also be significant for aircraft performing circling movements and roll-stabilized guided weapons. A common mistake is to estimate scale factor errors, but not cross-coupling errors as they are usually of a similar magnitude. For very high-precision applications, gravity modeling errors may be estimated.

The Kalman filter may also estimate errors exhibited by other components of an integrated navigation system, such as GNSS clock errors [3, 19, 36]. However, this is outside the scope of this article.

For the integration/alignment algorithm described in the following subsections, the INS attitude and velocity errors, resolved in north, east and down axes; the position error expressed in terms of latitude, longitude, and height; and the accelerometer and gyro biases are estimated. The state vector is thus

$$\mathbf{x} = \begin{pmatrix} \delta\boldsymbol{\psi}_{nb}^{n} \\ \delta\mathbf{v}_{eb}^{n} \\ \delta\mathbf{p}_{b} \\ \mathbf{b}_{a} \\ \mathbf{b}_{g} \end{pmatrix}, \qquad \delta\mathbf{p}_{b} = \begin{pmatrix} \delta L_{b} \\ \delta\lambda_{b} \\ \delta h_{b} \end{pmatrix}. \tag{67}$$

C. System Propagation

The system model is used to propagate forward the Kalman filter state estimates and their associated error covariance, from one epoch in time to the next. The state estimates are propagated using

$$\hat{\mathbf{x}}_k^- = \mathbf{\Phi}_{k-1}\hat{\mathbf{x}}_{k-1}^+ , \qquad (68)$$

where $\hat{\mathbf{x}}_k^-$ is the vector of state estimates at epoch k prior to the incorporation of measurement information, $\hat{\mathbf{x}}_{k-1}^+$ is the vector of state estimates at epoch $k-1$ after the measurement update, and $\mathbf{\Phi}_{k-1}$ is the transition matrix from epoch $k-1$ to epoch k.

The transition matrix is derived from the dynamic model,

$$\dot{\mathbf{x}}(t) = \mathbf{F}(t)\mathbf{x}(t) + \mathbf{G}(t)\mathbf{w}_s(t) , \qquad (69)$$

where $\mathbf{F}$ is the system matrix, $\mathbf{G}$ is the system noise distribution matrix and $\mathbf{w}_s$ is the system noise vector. A key assumption of this model is thus that the time derivative of each state is a linear function of the other states and white Gaussian noise sources. For integration and alignment of most inertial navigation systems, these assumptions are approximately correct. For short time intervals, the transition matrix may be approximated to [3, 35–38]

$$\mathbf{\Phi}_{k-1} \approx \mathbf{I} + \mathbf{F}_{k-1}\tau_s . \qquad (70)$$

where τ_s is the time interval between successive epochs.

For INS integration and alignment, much of the system model for the state vector defined in (67) is intuitive. The rate of change of the attitude error is dominated by the gyro bias, the rate of change of the velocity error is dominated by the accelerometer bias and the rate of change of the position error is dominated by the velocity error. However, additional dependencies must be modeled due to the rotation of the north, east, and down axes with respect to the Earth as the system moves; the rotation of the Earth with respect to inertial space; and the variation of gravity with height. The derivation of the system model is fully described in [3, 19]. Here, only the result is presented. The system matrix is

$$\mathbf{F} = \begin{pmatrix} \mathbf{F}_{11}^n & \mathbf{F}_{12}^n & \mathbf{F}_{13}^n & \mathbf{0}_3 & \hat{\mathbf{C}}_b^n \\ \mathbf{F}_{21}^n & \mathbf{F}_{22}^n & \mathbf{F}_{23}^n & \hat{\mathbf{C}}_b^n & \mathbf{0}_3 \\ \mathbf{0}_3 & \mathbf{F}_{32}^n & \mathbf{F}_{33}^n & \mathbf{0}_3 & \mathbf{0}_3 \\ \mathbf{0}_3 & \mathbf{0}_3 & \mathbf{0}_3 & \mathbf{0}_3 & \mathbf{0}_3 \\ \mathbf{0}_3 & \mathbf{0}_3 & \mathbf{0}_3 & \mathbf{0}_3 & \mathbf{0}_3 \end{pmatrix} , \qquad (71)$$

where

$$\mathbf{F}_{11}^n = -\left[\left(\hat{\boldsymbol{\omega}}_{ie}^n + \hat{\boldsymbol{\omega}}_{en}^n\right)\wedge\right] \qquad \hat{\boldsymbol{\omega}}_{ie}^n = \omega_{ie}\begin{pmatrix} \cos\hat{L}_b \\ 0 \\ -\sin\hat{L}_b \end{pmatrix} , \qquad (72)$$

$$\mathbf{F}_{12}^n = \begin{bmatrix} 0 & \dfrac{-1}{R_E(\hat{L}_b)+\hat{h}_b} & 0 \\[3mm] \dfrac{1}{R_N(\hat{L}_b)+\hat{h}_b} & 0 & 0 \\[3mm] 0 & \dfrac{\tan\hat{L}_b}{R_E(\hat{L}_b)+\hat{h}_b} & 0 \end{bmatrix},$$

(73)

$$\mathbf{F}_{13}^n = \begin{bmatrix} \omega_{ie}\sin\hat{L}_b & 0 & \dfrac{\hat{v}_{eb,E}^n}{\left(R_E(\hat{L}_b)+\hat{h}_b\right)^2} \\[4mm] 0 & 0 & \dfrac{-\hat{v}_{eb,N}^n}{\left(R_N(\hat{L}_b)+\hat{h}_b\right)^2} \\[4mm] \omega_{ie}\cos\hat{L}_b + \dfrac{\hat{v}_{eb,E}^n}{\left(R_E(\hat{L}_b)+\hat{h}_b\right)\cos^2\hat{L}_b} & 0 & \dfrac{-\hat{v}_{eb,E}^n\tan\hat{L}_b}{\left(R_E(\hat{L}_b)+\hat{h}_b\right)^2} \end{bmatrix},$$

(74)

$$\mathbf{F}_{21}^n = -\left[\left(\hat{\mathbf{C}}_b^n\hat{\mathbf{f}}_{ib}^b\right)\wedge\right],$$

(75)

$$\mathbf{F}_{22}^n = \begin{bmatrix} \dfrac{\hat{v}_{eb,D}^n}{R_N(\hat{L}_b)+\hat{h}_b} & -\dfrac{2\hat{v}_{eb,E}^n\tan\hat{L}_b}{R_E(\hat{L}_b)+\hat{h}_b}-2\omega_{ie}\sin\hat{L}_b & \dfrac{\hat{v}_{eb,N}^n}{R_N(\hat{L}_b)+\hat{h}_b} \\[4mm] \dfrac{\hat{v}_{eb,E}^n\tan\hat{L}_b}{R_E(\hat{L}_b)+\hat{h}_b}+2\omega_{ie}\sin\hat{L}_b & \dfrac{\hat{v}_{eb,N}^n\tan\hat{L}_b+\hat{v}_{eb,D}^n}{R_E(\hat{L}_b)+\hat{h}_b} & \dfrac{\hat{v}_{eb,E}^n}{R_E(\hat{L}_b)+\hat{h}_b}+2\omega_{ie}\cos\hat{L}_b \\[4mm] -\dfrac{2\hat{v}_{eb,N}^n}{R_N(\hat{L}_b)+\hat{h}_b} & -\dfrac{2\hat{v}_{eb,E}^n}{R_E(\hat{L}_b)+\hat{h}_b}-2\omega_{ie}\cos\hat{L}_b & 0 \end{bmatrix},$$

(76)

$$\mathbf{F}_{23}^n = \begin{bmatrix} -\dfrac{(\hat{v}_{eb,E}^n)^2\sec^2\hat{L}_b}{R_E(\hat{L}_b)+\hat{h}_b}-2\hat{v}_{eb,E}^n\omega_{ie}\cos\hat{L}_b & 0 & \dfrac{(\hat{v}_{eb,E}^n)^2\tan\hat{L}_b}{\left(R_E(\hat{L}_b)+\hat{h}_b\right)^2}-\dfrac{\hat{v}_{eb,N}^n\hat{v}_{eb,D}^n}{\left(R_N(\hat{L}_b)+\hat{h}_b\right)^2} \\[4mm] \left(\begin{array}{l}\dfrac{\hat{v}_{eb,N}^n\hat{v}_{eb,E}^n\sec^2\hat{L}_b}{R_E(\hat{L}_b)+\hat{h}_b}+2\hat{v}_{eb,N}^n\omega_{ie}\cos\hat{L}_b \\ -2\hat{v}_{eb,D}^n\omega_{ie}\sin\hat{L}_b\end{array}\right) & 0 & -\dfrac{\hat{v}_{eb,N}^n\hat{v}_{eb,E}^n\tan\hat{L}_b+\hat{v}_{eb,E}^n\hat{v}_{eb,D}^n}{\left(R_E(\hat{L}_b)+\hat{h}_b\right)^2} \\[4mm] 2\hat{v}_{eb,E}^n\omega_{ie}\sin\hat{L}_b & 0 & \dfrac{(\hat{v}_{eb,E}^n)^2}{\left(R_E(\hat{L}_b)+\hat{h}_b\right)^2}+\dfrac{(\hat{v}_{eb,N}^n)^2}{\left(R_N(\hat{L}_b)+\hat{h}_b\right)^2}-\dfrac{2g_0(\hat{L}_b)}{r_{eS}^e(\hat{L}_b)} \end{bmatrix},$$

(77)

$$r_{eS}^e\left(\hat{L}_b\right) = R_E\left(\hat{L}_b\right)\sqrt{1-e(2-e)\sin^2\hat{L}_b},$$

(78)

$$\mathbf{F}_{32}^n = \begin{bmatrix} \dfrac{1}{R_N(\hat{L}_b) + \hat{h}_b} & 0 & 0 \\ 0 & \dfrac{1}{\left(R_E(\hat{L}_b) + \hat{h}_b\right)\cos\hat{L}_b} & 0 \\ 0 & 0 & -1 \end{bmatrix}, \tag{79}$$

$$\mathbf{F}_{33}^n = \begin{bmatrix} 0 & 0 & -\dfrac{\hat{v}_{eb,N}^n}{\left(R_N(\hat{L}_b) + \hat{h}_b\right)^2} \\ \dfrac{\hat{v}_{eb,E}^n \sin\hat{L}_b}{\left(R_E(\hat{L}_b) + \hat{h}_b\right)\cos^2\hat{L}_b} & 0 & -\dfrac{\hat{v}_{eb,E}^n}{\left(R_E(\hat{L}_b) + \hat{h}_b\right)^2 \cos\hat{L}_b} \\ 0 & 0 & 0 \end{bmatrix}. \tag{80}$$

In each case, the caret, '^' denotes the navigation solution corrected using the most recent Kalman filter state estimates, $\hat{\mathbf{x}}_{k-1}^+$, as described in Section VI.E. Note that R_E is given by (29), R_N by (39), and g_0 by (43).

Moving from continuous to discrete time, from (70), the transition matrix may be approximated to

$$\boldsymbol{\Phi} \approx \begin{bmatrix} \mathbf{I}_3 + \mathbf{F}_{11}^n \tau_s & \mathbf{F}_{12}^n \tau_s & \mathbf{F}_{13}^n \tau_s & \mathbf{0}_3 & \hat{\mathbf{C}}_b^n \tau_s \\ \mathbf{F}_{21}^n \tau_s & \mathbf{I}_3 + \mathbf{F}_{22}^n \tau_s & \mathbf{F}_{23}^n \tau_s & \hat{\mathbf{C}}_b^n \tau_s & \mathbf{0}_3 \\ \mathbf{0}_3 & \mathbf{F}_{32}^n \tau_s & \mathbf{I}_3 + \mathbf{F}_{33}^n \tau_s & \mathbf{0}_3 & \mathbf{0}_3 \\ \mathbf{0}_3 & \mathbf{0}_3 & \mathbf{0}_3 & \mathbf{I}_3 & \mathbf{0}_3 \\ \mathbf{0}_3 & \mathbf{0}_3 & \mathbf{0}_3 & \mathbf{0}_3 & \mathbf{I}_3 \end{bmatrix}, \tag{81}$$

which is typically acceptable for propagation intervals of 0.2s or less.

At the same time as the state estimates are propagated forward in time using (68), the associated error covariance matrix is propagated using

$$\mathbf{P}_k^- = \boldsymbol{\Phi}_{k-1}\mathbf{P}_{k-1}^+ \boldsymbol{\Phi}_{k-1}^{\mathrm{T}} + \mathbf{Q}_{k-1}, \tag{82}$$

where $\mathbf{P}_k^-$ is the state error covariance matrix at epoch k prior to the incorporation of measurement information, $\mathbf{P}_{k-1}^+$ is the error covariance matrix at epoch $k-1$ after the measurement update, and $\mathbf{Q}_{k-1}$ is the system noise covariance matrix, which defines how the uncertainties of the state estimates increase with time, in this case, due to inertial sensor noise and bias variation.

For short propagation intervals ($\tau_s \leq 0.2$ s), a suitable system noise covariance matrix is

$$\mathbf{Q} \approx \begin{pmatrix} S_{rg}\mathbf{I}_3 & \mathbf{0}_3 & \mathbf{0}_3 & \mathbf{0}_3 & \mathbf{0}_3 \\ \mathbf{0}_3 & S_{ra}\mathbf{I}_3 & \mathbf{0}_3 & \mathbf{0}_3 & \mathbf{0}_3 \\ \mathbf{0}_3 & \mathbf{0}_3 & \mathbf{0}_3 & \mathbf{0}_3 & \mathbf{0}_3 \\ \mathbf{0}_3 & \mathbf{0}_3 & \mathbf{0}_3 & S_{bad}\mathbf{I}_3 & \mathbf{0}_3 \\ \mathbf{0}_3 & \mathbf{0}_3 & \mathbf{0}_3 & \mathbf{0}_3 & S_{bgs}\mathbf{I}_3 \end{pmatrix} \tau_s, \tag{83}$$

where S_{rg}, S_{ra}, S_{bad}, and S_{bgd} are the power spectral densities of, respectively, the gyro random noise, accelerometer random noise, accelerometer bias variation, and gyro bias variation, and it is assumed that all gyros and all accelerometers have equal noise characteristics. Values may be obtained from the inertial sensor manufacturer's specifications or from laboratory tests. However, in practice, some trial and error is often needed to determine the best values, particularly as the system noise covariance must also account for the effects of unestimated systematic errors, such as the scale factor and cross-coupling errors.

D. Measurement Update

The measurement update phase of the Kalman filter updates the state estimates using information from the measurements. For the INS integration/alignment example presented here, the measurements comprise position and velocity from an aiding system, such as GNSS. This position-domain integration is sometimes referred to as a loosely-coupled architecture and may also incorporate attitude measurements, where available. In the alternative tightly-coupled architecture, ranging, displacement, bearing and elevation, and/or line fix measurements are used [3, 19]. Tightly-coupled integration offers more flexibility and normally leads to a more accurate and robust navigation solution. However, it can only be implemented where the aiding system outputs the necessary information.

The measurement innovation, $\delta \mathbf{z}^-$, comprises the difference between the true measurement vector, $\mathbf{z}$, and that estimated from the state vector prior to the measurement update. Thus, for the example presented here, the measurement innovation is the difference between the position and velocity from the aiding system and the corrected INS position and velocity solution:

$$\delta \mathbf{z}_k^- = \begin{pmatrix} \mathbf{S}_p \left(\hat{\mathbf{p}}_a - \hat{\mathbf{p}}_b - \hat{\mathbf{T}}_{r(n)}^p \hat{\mathbf{C}}_b^n \mathbf{l}_{ba}^b \right) \\ \hat{\mathbf{v}}_{ea}^n - \hat{\mathbf{v}}_{eb}^n - \hat{\mathbf{C}}_b^n \left(\hat{\boldsymbol{\omega}}_{ib}^b \wedge \mathbf{l}_{ba}^b \right) + \hat{\boldsymbol{\Omega}}_{ie}^n \hat{\mathbf{C}}_b^n \mathbf{l}_{ba}^b \end{pmatrix}_k , \tag{84}$$

where k is the current epoch; $\hat{\mathbf{p}}_a = \begin{pmatrix} \hat{L}_a & \hat{\lambda}_a & \hat{h}_a \end{pmatrix}^{\mathrm{T}}$ and $\hat{\mathbf{p}}_b = \begin{pmatrix} \hat{L}_b & \hat{\lambda}_b & \hat{h}_b \end{pmatrix}^{\mathrm{T}}$ are, respectively, the aiding system and INS curvilinear position solutions; $\hat{\mathbf{v}}_{ea}^n$ and $\hat{\mathbf{v}}_{eb}^n$ are, respectively, the aiding system and INS velocity solutions; $\hat{\mathbf{C}}_b^n$ is the INS attitude solution; $\hat{\boldsymbol{\omega}}_{ib}^b$ is the INS angular rate; $\mathbf{l}_{ba}^b$ is the lever arm from the INS to the aiding sensor; $\hat{\boldsymbol{\Omega}}_{ie}^n$ is obtained from (37) using the INS latitude solution; $\hat{\mathbf{T}}_{r(n)}^p$, given by

$$\hat{\mathbf{T}}_{r(n)}^p = \frac{\partial \mathbf{p}_b}{\partial \mathbf{r}_{eb}^n} = \begin{pmatrix} \dfrac{1}{R_N(\hat{L}_b) + \hat{h}_b} & 0 & 0 \\ 0 & \dfrac{1}{\left(R_E(\hat{L}_b) + \hat{h}_b\right) \cos \hat{L}_b} & 0 \\ 0 & 0 & -1 \end{pmatrix}, \tag{85}$$

is used to convert position perturbations from Cartesian to curvilinear; and $\mathbf{S}_p$ is the curvilinear position scaling matrix, given by

$$\mathbf{S}_p = \begin{pmatrix} s_{L\lambda} & 0 & 0 \\ 0 & s_{L\lambda} & 0 \\ 0 & 0 & 1 \end{pmatrix}, \tag{86}$$

where a suitable value for $s_{L\lambda}$ is 10^3. This prevents numerical problems.

The Kalman filter measurement update is then performed in three steps:

$$\mathbf{K}_k = \mathbf{P}_k^- \mathbf{H}_k^{\mathrm{T}} \left(\mathbf{H}_k \mathbf{P}_k^- \mathbf{H}_k^{\mathrm{T}} + \mathbf{R}_k \right)^{-1}, \tag{87}$$

$$\hat{\mathbf{x}}_k^+ = \hat{\mathbf{x}}_k^- + \mathbf{K}_k \delta \mathbf{z}_k^-, \tag{88}$$

$$\mathbf{P}_k^+ = \left(\mathbf{I} - \mathbf{K}_k \mathbf{H}_k \right) \mathbf{P}_k^-, \tag{89}$$

where $\mathbf{K}_k$ is the Kalman gain matrix, $(\ )^{-1}$ denotes matrix inversion, and the measurement matrix can normally be approximated to

$$\mathbf{H}_k \approx \begin{pmatrix} \mathbf{0}_3 & \mathbf{0}_3 & -\mathbf{S}_p & \mathbf{0}_3 & \mathbf{0}_3 \\ \mathbf{0}_3 & -\mathbf{I}_3 & \mathbf{0}_3 & \mathbf{0}_3 & \mathbf{0}_3 \end{pmatrix}, \tag{90}$$

as the coupling of the attitude errors and gyro biases into the measurements through the lever arm is normally weak.

The diagonal components of the measurement noise covariance matrix, $\mathbf{R}_k$, are the variances of the noise on each component of the position and velocity solution from the aiding system, such as GNSS. Where known, any correlation between the different components should be modeled using the off-diagonal elements of $\mathbf{R}_k$. Furthermore, where this measurement noise is correlated over time, it is necessary to increase $\mathbf{R}_k$ accordingly, multiplying it by the ratio of the correlation time to the update interval. In practice, some trial and error is needed to determine the best values.

E. Navigation Solution Correction

The final step in each cycle of an integration or alignment algorithm is to correct the position, velocity, and attitude solution using

$$\hat{\mathbf{C}}_b^n(+) = \left(\mathbf{I}_3 - \left[\delta \hat{\boldsymbol{\psi}}_{nb}^n \wedge \right] \right) \hat{\mathbf{C}}_b^n(-), \tag{91}$$

$$\hat{\mathbf{v}}_{eb}^n(+) = \hat{\mathbf{v}}_{eb}^n(-) - \delta \hat{\mathbf{v}}_{eb}^n \tag{92}$$

and

$$\begin{aligned} \hat{L}_b(+) &= \hat{L}_b(-) - \delta \hat{L}_b \\ \hat{\lambda}_b(+) &= \hat{\lambda}_b(-) - \delta \hat{\lambda}_b, \\ \hat{h}_b(+) &= \hat{h}_b(-) - \delta \hat{h}_b \end{aligned} \tag{93}$$

where the suffixes $(-)$ and $(+)$ denote before and after the correction, respectively, and the small angle approximation is assumed to be applicable to the attitude error. Following these corrections, the attitude error, velocity error, and position error states of the Kalman filter are zeroed as the information they contain has been transferred to the navigation solution. However, the error covariance matrix, $\mathbf{P}$, remains unchanged, because the error in the state estimates has not changed.

The accelerometer and gyro biases estimated by the Kalman filter are also fed back to correct the IMU measurements as they are input to the inertial navigation equations. These corrections are in addition to any that may be applied by the IMU's processor. These accelerometer and gyro corrections must be applied on every

iteration of the navigation equations, with feedback from the Kalman filter periodically updating them. Consequently, the accelerometer and gyro bias estimates are commonly stored in the navigation processor with the Kalman filter estimating the residual errors and feeding back perturbations to the biases stored by the navigation processor. The Kalman filter bias estimates are zeroed each time they are used to estimate the navigation processor's bias estimates.

VII. ZERO UPDATES AND MOTION CONSTRAINTS

Zero updates and motion constraints, also known as nonholonomic constraints, use information about the host vehicle (or user) motion to correct the inertial navigation solution and calibrate the sensor errors. They may be processed as Kalman filter measurements in the same way as aiding sensor measurements in an integrated navigation system (Section VI) and may share the same Kalman filter. They are particularly useful where GNSS reception is poor. The zero velocity update (ZVU or ZUPT), zero angular rate update (ZARU), land vehicle motion constraints, and pedestrian motion constraints are described in turn.

A. Zero Velocity Updates

Zero velocity updates are useful for any application where the host vehicle or user is often stationary during navigation, such as land vehicle navigation [39] (without odometry, which provides velocity continuously). For pedestrian navigation with a shoe-mounted IMU, a ZVU may be performed on every step. When combined with a method for reducing heading drift, this enables relatively accurate inertial navigation to be performed with very-low-cost consumer-grade inertial sensors [40–42]. Other applications of ZVUs include robotics, helicopter navigation (during touchdowns), and inertial surveying.

The measurement innovation for a ZVU is simply

$$\delta \mathbf{z}_k^- = -\hat{\mathbf{v}}_{eb,k}^n \tag{94}$$

and the measurement matrix, assuming the state vector defined by (67), is

$$\mathbf{H}_k = \begin{pmatrix} \mathbf{0}_3 & -\mathbf{I}_3 & \mathbf{0}_3 & \mathbf{0}_3 & \mathbf{0}_3 \end{pmatrix}. \tag{95}$$

Although ZVUs do not provide absolute position information, the Kalman filter models the correlation between the velocity and position errors in the off-diagonal elements of the error covariance matrix, $\mathbf{P}$. This enables a ZVU to correct most of the position drift since the last measurement update, ZVU or otherwise [28].

Measurement noise arises due to vibration and disturbances. Vehicles may be disturbed by wind gusts, other vehicles passing, people moving around inside, loading, and unloading. Similarly, a nominally-stationary pedestrian may be moving on the spot. The amount of residual motion during a ZVU will depend on what the stationary-condition detection algorithm allows, so there should be a relationship between the assumed measurement noise covariance and the detection threshold.

For extended stationary periods, e.g. during initialization of an aircraft navigation system, zero position displacement measurements can give better performance. The measurement innovation is

$$\delta \mathbf{z}_k^- = \mathbf{S}_p \big(\hat{\mathbf{p}}_b(t_0) - \hat{\mathbf{p}}_b(t) \big), \tag{96}$$

where t_0 is the time when the system first became stationary or the initialization time, as appropriate, and $\mathbf{S}_p$ is given by (86). The measurement matrix is

$$\mathbf{H}_k = \begin{pmatrix} \mathbf{0}_3 & \mathbf{0}_3 & -\mathbf{S}_p & \mathbf{0}_3 & \mathbf{0}_3 \end{pmatrix}. \tag{97}$$

ZVUs must only be performed when the navigation system is stationary. For surveying applications, stationarity is typically indicated by the operator. However, for navigation, automated detection is needed. Pedestrians may be assumed to be stationary if the magnitude of the accelerometer measurements is close to the acceleration due to gravity for about 0.5s for body-mounted sensors and 0.2s for foot-mounted sensors [28, 42]. This is because most parts of the body are constantly accelerating and decelerating during walking and running. The horizontal velocity solution is typically used to determine when a land vehicle is stationary, with accelerometer or gyro measurements used for confirmation [39, 43].

B. Zero Angular Rate Update

A zero angular rate update is useful for low-performance gyros with errors at least as large as the angular disturbances to a stationary vehicle or person. ZARUs and ZVUs are sometimes performed separately and sometimes performed together. For land vehicle applications, zero angular rate may be assumed whenever the vehicle is stationary. For pedestrian applications, ZARUs should be approached with caution because the residual angular motion of a stationary person's body can be much larger than the gyro errors, while a foot can rotate during the stance phase of walking. An additional test is therefore needed to determine whether a ZARU should be performed.

The measurement innovation for a full-IMU ZARU is

$$\delta \mathbf{z}_k^- = -\hat{\boldsymbol{\omega}}_{ib,k}^b. \tag{98}$$

Assuming the state vector defined by (67), the measurement matrix is simply

$$\mathbf{H}_k = \begin{pmatrix} \mathbf{0}_3 & \mathbf{0}_3 & \mathbf{0}_3 & \mathbf{0}_3 & -\mathbf{I}_3 \end{pmatrix}. \tag{99}$$

The measurement noise covariance represents the variance of the nominally-zero angular rate due to vibration and disturbances. For a stationary land vehicle, there will be less disturbance about the yaw axis than about the roll and pitch axes.

C. Land Vehicle Motion Constraints

Normal land vehicle motion is subject to two constraints. The velocity of the vehicle is zero along the rotation axis of any of its wheels and is also zero in the direction perpendicular to the road or rail surface [44, 45]. The acceleration is not necessarily zero. This vehicle velocity constraint can be applied as a Kalman filter measurement update with measurement innovation

$$\delta \mathbf{z}_k^- = -\begin{pmatrix} 0 & 1 & 0 \\ 0 & 0 & 1 \end{pmatrix}\left(\hat{\mathbf{C}}_n^b \hat{\mathbf{v}}_{eb}^n - \hat{\boldsymbol{\omega}}_{ib}^b \wedge \mathbf{l}_{rb}^b \right), \tag{100}$$

where $\mathbf{l}_{rb}^b$ is the lever arm from the center of the rear axle to the origin of the IMU body frame, resolved along the IMU axes, which are assumed here to be aligned with the forward, right and down directions of the vehicle body. Assuming the state vector defined by (67) and neglecting the coupling of the attitude errors and gyro biases into the measurements through the lever arm, the measurement matrix may be approximated to

$$\mathbf{H}_k \approx \begin{pmatrix} \mathbf{0}_{2\times 3} & -\begin{pmatrix} 0 & 1 & 0 \\ 0 & 0 & 1 \end{pmatrix} \hat{\mathbf{C}}_n^b & \mathbf{0}_{2\times 3} & \mathbf{0}_{2\times 3} & \mathbf{0}_{2\times 3} \end{pmatrix}. \tag{101}$$

This is equivalent to a ZVU applied along only two axes. However, the motion-constraint measurements may be applied continuously. If the IMU is not aligned with the vehicle body, the relative orientation may be estimated by the Kalman filter, as may the lever arm [46, 47].

The measurement noise covariance must account for the differences between the true and assumed vehicle motion. Causes include sideslip of the wheels, the vehicle's suspension system, and engine vibration [44]. The time correlation of these effects may be significant where the measurement update rate is high.

Sideslip can invalidate the transverse velocity constraint when the vehicle turn rate exceeds about 0.05 rad s^{-1}. Better performance is therefore obtained if the transverse measurements are omitted whenever the yaw rate exceeds a pre-defined threshold [48].

D. Pedestrian Motion Constraints

In man-made environments, pedestrians tend to walk in approximately straight lines, particularly where walls and roads are in the way. Therefore, the drift in an inertial navigation solution can be constrained by assuming that a person's heading is constant whenever the change in the INS heading solution over a certain interval is below a certain threshold [49]. Indoors, the floor is usually flat, so a constant-height constraint may be assumed unless steps, an escalator, an elevator, or a ramp are detected [50].

VIII. PEDESTRIAN DEAD RECKONING USING STEP DETECTION

Pedestrian navigation is highly challenging. It must work in urban areas, under tree cover, and indoors, where coverage of GNSS and many other radio navigation systems is poor. Inertial sensors can be used to measure motion. However, for pedestrian use, they must be small, light, consume minimal power, and, for most applications, be low-cost, requiring MEMS sensors to be used. However, these provide very poor inertial navigation performance stand alone, while the combination of low dynamics and high vibration makes them difficult to calibrate using other positioning systems. One option is to use a shoe-mounted IMU with conventional inertial navigation (Section IV) aided by zero velocity updates (Section VII.A) every step. However, this is impractical for many applications.

This section describes pedestrian dead reckoning (PDR) using step detection, whereby the inertial sensors are used for detecting steps. Note that a step is the movement of one foot with the other remaining stationary, while a stride is the successive movement of both feet. This gives significantly better performance than conventional inertial navigation for sensors mounted on the user's body or in a handheld device, even with tactical-grade sensors [28].

As shown in Figure 20, a PDR algorithm comprises three phases: step detection, step length estimation, and navigation-solution update. The step-detection phase identifies that a step has taken place. For body-mounted or device-mounted sensors, the vertical or root sum of squares (RSS) accelerometer signals exhibit a double-peaked oscillatory pattern. Steps can be detected from the peaks [51] or the

points where the specific force rises above or drops below the acceleration due to gravity [52], with a recognition window used to limit false detections.
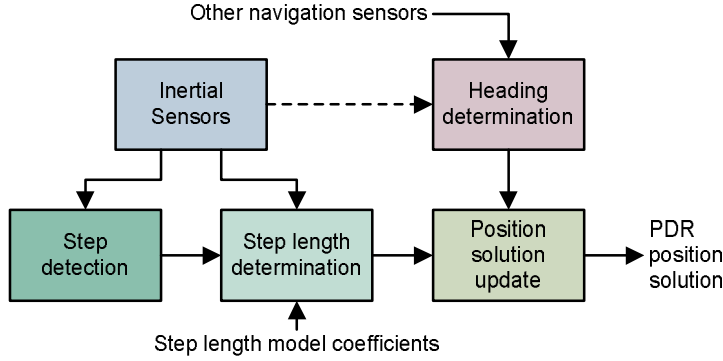

Figure 20. Pedestrian dead reckoning processing. (From [3] © Paul Groves 2013. Reproduced with Permission).

The step length varies depending on the individual, the slope and texture of the terrain, whether there are obstacles to be negotiated, whether an individual is tired, whether they are carrying things, and whether they are walking alone or with others. Thus, PDR implementations that assume a fixed step length for each user are only accurate to about 10 percent of distance traveled [53]. However, the step length may be modeled as a function of parameters such as the step frequency, the variance of the accelerometer measurements, the slope of the terrain, and the vertical velocity. One model is [42]:

$$\Delta r_P = c_{P0} + \frac{c_{P1}}{\tau_P} + c_{P2}\sigma_f^2 + c_{P3}\hat{\theta}_{nb} , \tag{102}$$

where Δr_P is the PDR-estimated step length, τ_P is the interval between successive steps, σ_f^2 is the variance of the specific force measurements, $\hat{\theta}_{nb}$, is the estimated angle of the slope, and c_{P0}, c_{P1}, c_{P2}, and c_{P3} are the model coefficients. Using this approach, an accuracy of about 3 percent of distance traveled may be obtained [54, 55]. The model coefficients for each user may be estimated using measurements from GNSS or another positioning system.

How inertial sensors respond to pedestrian motion depends on their location. Thus, an algorithm optimized for waist-mounted sensors may not give the best results for sensors located in a pocket, in a backpack, or in a device held by the user. Similarly, step-length model coefficients optimized for walking will not give good results for running, turning and climbing stairs or steps. A robust implementation of PDR should thus incorporate a real-time classification system that detects both the motion type and sensor location and tunes both the step-detection and step-length-estimation algorithms accordingly [56, 57].

IX. FAULT DETECTION

There are a number of ways in which an inertial navigation system can fail. Faults can arise in individual inertial sensors. All inertial sensors can exhibit large errors when the vibration levels are much higher than the system is designed for or

there is a mounting failure. The whole IMU or INS may also exhibit a power failure, software failure, or communications failure, which can sometimes be fixed by performing a reset.

To avoid producing a false navigation solution, fault detection is required. The simplest approach is range checks, which may be applied to both the sensor measurements and the navigation solution. Faulty sensors may output measurements outside the operational range specified by the manufacturer or the operating range of the sensor environment. A faulty sensor can also produce a succession of repeated measurements, null measurements or no measurements at all.

A fault may also be indicated by a navigation solution outside the operational envelope of the application. Every vehicle has a maximum speed, a land vehicle or ship should always be close to the Earth's surface, and every aircraft has a maximum altitude above which it cannot fly.

Where a Kalman filter is used to align and calibrate the INS and/or integrate it with other sensors, as described in Section VI, it may also be used for fault detection. The accelerometer and gyro biases are normally estimated as states. Therefore, if a bias estimate is several times the standard deviation specified by the manufacturer, there is likely to be a fault with the sensor. Outlying state estimates can also arise due to a lack of measurements or observability problems. However, in these cases, the state uncertainties will also be large.

The Kalman filter measurement innovations, $\delta\mathbf{z}_k^-$, provide an indication of whether the measurements and state estimates are consistent with each other. Therefore, by comparing the current innovations with their expected uncertainties and computing statistics over several epochs, errors in both the INS and the aiding sensors may be detected [3].

Where a standard IMU with three accelerometers and three gyros is used, the whole inertial navigation solution must normally be discarded if a fault is found in one of the sensors. However, if additional sensors are included, a navigation solution may be maintained. These systems are known as redundant IMUs [58, 59]. The sensors are normally mounted in a skewed configuration so that all six degrees of freedom can be observed using any three accelerometers and any three gyros. Where external information is available for fault detection, recovery from faults is achievable using four accelerometers and four gyros.

The outputs of four skewed accelerometers or gyros may be compared with each other to determine if they are in agreement. This is known as consistency checking [3] and can detect a fault without external information. However, it cannot identify the faulty sensor. This requires five accelerometers and gyros, enabling different combinations of four sensors to be tested for consistency. If a fault is detected immediately, the inertial navigation solution may be protected simply by excluding further measurements from the faulty sensor. However, to protect against slow-onset faults, parallel inertial navigation solutions computed from different sensor combinations must be maintained.

X. CONCLUDING REMARKS

Inertial sensors have been used in navigation for many decades. However, the field is still evolving. The development of small, light, low-cost sensors has greatly

expanded the number of applications. At the same time, advances such as GNSS integration, step detection, and context-specific motion constraints has enabled better navigation performance to be extracted from lower quality sensors. Looking to the future, developments in accelerometer and gyro technology are likely to offer higher performance at lower cost. At the same time, new navigation and positioning techniques are being developed for use alongside inertial sensors in integrated systems [60].

Further details on all of the topics covered in this tutorial may be found in [3] and the references therein, some of which are listed below.

References

[1] T. F. Weiner, *Theoretical Analysis of Gimballess Inertial Reference Equipment using Delta-Modulated Instruments*, Doctor of Science Thesis, Massachusetts Institute of Technology, Cambridge, MA, 1962.

[2] P. G. Savage, "Blazing Gyros: The Evolution of Strapdown Inertial Navigation Technology for Aircraft," *Journal of Guidance, Control, and Dynamics*, Vol. 35, pp. 637–655, May-June 2013.

[3] P. D. Groves, *Principles of GNSS, Inertial, and Multisensor Integrated Navigation Systems*, 2nd ed., Boston, MA: Artech House, 2013.

[4] D. H. Titterton and J. L. Weston, *Strapdown Inertial Navigation Technology*, 2nd ed., Stevenage, UK: IEE, 2004.

[5] A. Lawrence, *Modern Inertial Technology*, 2nd ed., New York: Springer-Verlag, 2001.

[6] V. Kempe, *Inertial MEMS Principles and Practices*, Cambridge, UK: Cambridge University Press, 2011.

[7] D. Karnick et al., "Honeywell Gun-hard Inertial Measurement Unit (IMU) Development," in *Institute of Navigation Nat. Technical Meeting*, San Diego, CA, Jan. 2007, pp. 718–724.

[8] H. J., McGuinness, A. K. Rakholia, and G. W. Biedermann, "High Data-Rate Atom Interferometer for Measuring Acceleration," *Applied Physics Letters*, Vol. 100, Article ID 011106, 2012.

[9] D., Brown, et al., "Atom Interferometric Gravity Sensor System," in *IEEE/ION Position Location and Navigation Symposium (PLANS)*, Myrtle Beach, SC, Apr. 2012, pp. 30–37.

[10] M. S. Grewal, L. R. Weill, and A. P. Andrews, *Global Positioning Systems, Inertial Navigation, and Integration*, 2nd ed., New York: Wiley, 2007.

[11] E. A. Donley, "Nuclear Magnetic Resonance Gyroscopes," in *IEEE Sensors 2010*, Waikoloa, HI, Nov. 2010, pp. 17–22.

[12] J. K. Stockton, K. Takase, and M. A. Kasevich, "Absolute Geodetic Rotation Measurement Using Atom Interferometry," *Physical Review Letters*, Vol. 107, Article ID 133001, 2011.

[13] E. Edwan, S. Knedlik, and O. Loffeld, "Constrained Angular Motion Estimation in a Gyro-Free IMU," *IEEE Trans. Aerosp. Electron Syst.*, Vol. 47, pp. 596–610, Jan. 2011.

[14] N. El-Sheimy, "The Potential of Partial IMUs for Land Vehicle Navigation," *Inside GNSS*, Spring 2008, pp. 16–25.

[15] S. J. Pethel, "Test and Evaluation of High Performance Micro Electro-Mechanical System Based Inertial Measurement Units," in *IEEE/ION Position Location and Navigation Symposium (PLANS)*, San Diego, CA, Apr. 2006, pp. 772–794.

[16] Y. Yuksel, N. El-Sheimy, and A. Noureldin, "Error Modeling and Characterization of Environmental Effects for Low Cost Inertial MEMS Units," in *IEEE/ION Position Location and Navigation Symposium (PLANS)*, Palm Springs, CA, May 2010, pp. 598–612.

[17] C. Jekeli, *Inertial Navigation Systems with Geodetic Applications*, Berlin, Germany: de Gruyter, 2000.

[18] P. G. Savage, *Strapdown Analytics parts 1 and 2*, Maple Plain, MN: Strapdown Associates, 2000.

[19] J. A. Farrell, *Aided Navigation*, New York: McGraw Hill, 2008.

[20] K. R. Britting, *Inertial Navigation Systems Analysis*, New York: Wiley, 1971. (Republished by Norwood, MA: Artech House, 2010)

[21] *Department of Defense World Geodetic System 1984*, National Imagery and Mapping Agency (now NGA), TR8350.2, Third Edition, 1997.

[22] J. Iliffe, and R. Lott, *Datums and Map Projections for Remote Sensing, GIS and Surveying*, 2nd ed., Edinburgh, UK: Whittles Publishing, 2008.

[23] P. G. Savage, "Strapdown Inertial Navigation Integration Algorithm Design Part 1: Attitude Algorithms," *Journal of Guidance Control and Dynamics*, Vol. 21, pp. 19–28, Jan.-Feb. 1998; Erratum: Vol. 22, p. 384, Mar.-Apr. 1999; "Strapdown Inertial Navigation Integration Algorithm Design Part 2: Velocity and Position Algorithms," *Journal of Guidance Control and Dynamics*, Vol. 21, pp. 208–221, Mar.-Apr. 1998; Erratum: Vol. 27, p. 318, Mar.-Apr. 2004.

[24] E. Levinson and R. Majure, "Accuracy Enhancement Techniques Applied to the Marine Ring Laser Inertial Navigator (MARLIN)," *NAVIGATION*, Vol. 34, pp. 64–86, Spring 1987.

[25] C. Hua, "Gyrocompass Alignment with Base Motions: Result for a 1nmi/h INS.GPS System," *NAVIGATION*, Vol. 47, pp. 65–74, Summer 2000.

[26] R. B. Langley, "Getting Your Bearings: The Magnetic Compass and GPS," *GPS World*, Sept. 2003, pp. 70–81.

[27] Y. Zhao, *Vehicle Location and Navigation Systems*, Norwood, MA: Artech House, 1997.

[28] C. J. Mather, P. D. Groves, and M. R. Carter, "A Man Motion Navigation System Using High Sensitivity GPS, MEMS IMU and Auxiliary Sensors," In. *Institute of Navigation GNSS 2006*, Fort Worth, TX, Sept. 2006, pp. 2704–2714.

[29] M. H. Afzal, *Use of Earth's Magnetic Field for Pedestrian Navigation*, PhD dissertation, University of Calgary, Calgary, July 2011.

[30] D. Gebre-Egziabher, et al., "Calibration of Strapdown Magnetometers in Magnetic Field Domain," *Journal of Aerospace Engineering*, Vol. 19, No. 2, 2006, pp. 87–102.

[31] P. Guo et al., "The Soft Iron and Hard Iron Calibration Method using Extended Kalman Filter for Attitude and Heading Reference System," in *IEEE/ION Position Location and Navigation Symposium (PLANS)*, Monterey, CA, May 2008, pp. 1167–1174

[32] M. Kayton, and W. G. Wing, "Attitude and Heading References," In *Avionics Navigation Systems*, 2nd ed., New York: Wiley, 1997, pp. 426–448.

[33] E. D. Kaplan, and C. J. Hegarty, *Understanding GPS Principles and Applications*, 2nd ed., Norwood, MA: Artech House, 2006.

[34] P. Misra, and P. Enge, *Global Positioning System Signals, Measurements, and Performance*, 2nd ed., Lincoln, MA: Ganga-Jamuna Press, 2006.

[35] A. Gelb, *Applied Optimal Estimation*, Cambridge, MA: MIT Press, 1974.

[36] R. G. Brown and P. Y. C. Hwang, *Introduction to Random Signals and Applied Kalman Filtering*, 3rd ed., New York: Wiley, 1997.

[37] M. S. Grewal, and A. P. Andrews, *Kalman Filtering: Theory and Practice*, 2nd ed., New York: Wiley, 2000.

[38] D. Simon, *Optimal State Estimation*, New York: Wiley, 2006.

[39] D. A. Grejner-Brzezinska, Y. Yi, and C. K. Toth, "Bridging Gaps in Urban Canyons: The Benefits of ZUPTS," *NAVIGATION*, Vol. 48, pp. 217–225, Winter 2001.

[40] E. Foxlin, "Pedestrian Tracking with Shoe-Mounted Inertial Sensors," *IEEE Comput. Graph. Appl.*, pp. 38–46, Nov.-Dec. 2005.

[41] S. Godha, G. Lachapelle, and M. E. Cannon, "Integrated GPS/INS System for Pedestrian Navigation in a Signal Degraded Environment," in *Institute of Navigation GNSS 2006*, Fort Worth, TX, Sept. 2006, pp. 2151–2164.

[42] P. D. Groves et al., "Inertial Navigation Versus Pedestrian Dead Reckoning: Optimizing the Integration," in *Institute of Navigation GNSS 2007*, Fort Worth, TX, Sept. 2007, pp. 2043–2055.

[43] P. Aggarwal et al., *MEMS-Based Integrated Navigation*, Norwood, MA: Artech House, 2010.

[44] G. Dissanayake, et al., "The Aiding of a Low-Cost Strapdown Inertial Measurement Unit Using Vehicle Model Constraints for Land Vehicle Applications," *IEEE Trans. Robot. Autom.*, Vol. 17, pp. 731–747, Oct. 2001.

[45] X. Niu, S. Nassar, and. N., El-Sheimy, "An Accurate Land-Vehicle MEMS IMU/GPS Navigation System using 3D Auxiliary Velocity Updates," *NAVIGATION*, Vol. 54, pp. 177–188, Fall 2007.

[46] Y. Wu., C. Goodall, and N. El-Sheimy, "Self-calibration for IMU/Odometer Land Navigation: Simulation and Test Results," in *Institute of Navigation International Technical Meeting*, San Diego, CA, Jan. 2010, pp. 839–849.

[47] E. Vinande, P. Axelrad, and D. Akos, "Mounting-Angle Estimation for Personal Navigation Devices," *IEEE Trans. Veh. Technol.*, Vol. 59, pp. 1129–1138, Mar. 2010.

[48] J. Ryan, and D. Bevly, "Robust Ground Vehicle Constraints for Aiding Stand Alone INS and Determining Inertial Sensor Errors," in *Institute of Navigation Int. Technical Meeting*, Newport Beach, CA, Jan. 2012, pp. 374–384.

[49] J. Borenstein, L. Ojeda, and S. Kwanmuang, "Heuristic Reduction of Gyro Drift for Personnel Tracking Systems," *Journal of Navigation*, Vol. 62, pp. 41–58, Jan. 2009.

[50] K. Abdulrahim et al., "Using Constraints for Shoe Mounted Indoor Pedestrian Navigation," *Journal of Navigation*, Vol. 65, pp. 15–28, Jan. 2012.

[51] T. Judd, "A Personal Dead Reckoning Module," in *Institute of Navigation GPS-97*, Kansas, MO, Sept. 1997, pp. 47–51.

[52] J. Käppi, J. Syrjärinne, and J. Saarinen, "MEMS-IMU Based Pedestrian Navigator for Handheld Devices," in *Institute of Navigation GPS 2001*, Salt Lake City, UT, Sept. 2001, pp. 1369–1373.

[53] J. Collin, O. Mezentsev, and G. Lachapelle, "Indoor Positioning System Using Accelerometry and High Accuracy Heading Sensors," in *Institute of Navigation GPS/GNSS 2003*, Portland, OR, Sept. 2003, pp. 1164–1170.

[54] Q. Ladetto, "On Foot navigation: continuous step calibration using both complementary recursive prediction and adaptive Kalman filtering," in *Institute of Navigation GPS 2000*, Salt Lake City, UT, Sept. 2000, pp. 1735–1740.

[55] H. Leppäkoski et al., "Error Analysis of Step Length Estimation in Pedestrian Dead Reckoning," in *Institute of Navigation GPS 2002*, Portland, OR, Sept. 2002, pp. 1136–1142.

[56] C. G. Park et al., "Adaptive Step Length Estimation with Awareness of Sensor Equipped Location for PNS," in *Institute of Navigation GNSS 2007*, Fort Worth, TX, Sept. 2007, pp. 1845–1850.

[57] L. Pei et al., "Using Motion-Awareness for the 3D Indoor Personal Navigation on a Smartphone," in *Institute of Navigation GNSS 2011*, Portland, OR, Sept. 2011, pp. 2906–2913.

[58] J. P. Gilmore and R. J. Cooper, *SIRU Development – Final Report Volume 1 System Development*, Charles Stark Draper Laboratory, Cambridge, MA,1973.

[59] S. Sukkarieh et al., "A Low-cost Redundant Inertial Measurement Unit for Unmanned Air Vehicles," *International Journal of Robotics Research*, Vol. 19, pp. 1089–1103, Nov. 2000.

[60] P. D. Groves, "The PNT Boom: Future Trends in Integrated Navigation," *Inside GNSS*, Mar.-Apr. 2013, pp. 44–49.

Author Biography

Dr Paul Groves has been researching navigation systems for 17 years. Since 2009, he has been a Lecturer (academic faculty member) at University College London (UCL). Previously, he worked as a research scientist at the Defence Evaluation and Research Agency and then QinetiQ. He is interested in all aspects of navigation and currently leads research into navigation using raw inertial sensors, pedestrian motion modeling, advanced integration architectures, navigation using novel environmental features, and GNSS shadow matching.

He is an author of more than 60 technical publications, including the book *Principles of GNSS, Inertial and Multi-Sensor Integrated Navigation Systems*, now in its second edition. He is a Fellow of the Royal Institute of Navigation and holds a bachelor's degree and doctorate in physics from the University of Oxford.